crystals

MDPI

Review

Review of Nanoindentation Size Effect: Experiments and Atomistic Simulation

George Z. Voyiadjis * and Mohammadreza Yaghoobi

Computational Solid Mechanics Laboratory, Department of Civil and Environmental Engineering, Louisiana State University, Baton Rouge, LA 70803, USA; myagho1@lsu.edu

* Correspondence: voyiadjis@eng.lsu.edu

Academic Editors: Helmut Cölfen and Ronald W. Armstrong

Received: 26 September 2017; Accepted: 20 October 2017; Published: 23 October 2017

Abstract: Nanoindentation is a well-stablished experiment to study the mechanical properties of materials at the small length scales of micro and nano. Unlike the conventional indentation experiments, the nanoindentation response of the material depends on the corresponding length scales, such as indentation depth, which is commonly termed the size effect. In the current work, first, the conventional experimental observations and theoretical models of the size effect during nanoindentation are reviewed in the case of crystalline metals, which are the focus of the current work. Next, the recent advancements in the visualization of the dislocation structure during the nanoindentation experiment is discussed, and the observed underlying mechanisms of the size effect are addressed. Finally, the recent computer simulations using molecular dynamics are reviewed as a powerful tool to investigate the nanoindentation experiment and its governing mechanisms of the size effect.

Keywords: nanoindentation; size effect; atomistic simulation; dislocation; grain boundary

1. Introduction

The size effect in material science is the variation of material properties as the sample characteristic length changes. In the current work, the focus is on the size effect on the nanoindentation response of crystalline metals. Nanoindentation is a well-stablished experiment to investigate the mechanical properties of material samples of small volumes. During the nanoindentation, a very hard tip is pressed into the sample, and the variation of load versus the penetration depth is recorded. In the case of nanoindentation, the dependency of material hardness on the corresponding characteristic length is termed as the size effect. The underlying mechanism of the size effect during nanoindentation depends on the material nature. In the case of crystalline metals, the size effect is governed by the dislocation-based mechanisms. The nanoindentation size effects in other materials such as ceramics, amorphous metals, polymers and semiconductor materials are controlled by cracking, non-dislocation-based mechanisms, shear transformation zones and phase transformations [1–4].

A very common size effect during the nanoindentation occurs in the case of the geometrically self-similar indenter tips. The conventional plasticity predicts that the hardness should be independent of the penetration depth. Experimental results, however, have shown that the hardness is a function of indentation depth, which is commonly termed as the indentation size effect [4–22]. The common size effect is the increase in hardness by decreasing the indentation depth. Most of the size effect studies support this trend. However, few studies have shown the inverse size effects in which as the indentation depth decreases, the hardness also decreases, which is commonly termed as inverse size effects [4–7,9,10,23]. However, the inverse size effect is commonly attributed to the artifacts of the experiment such as instrument vibration and the error in contact area measurements [4,8–10]. In addition to the size effect during the nanoindentation using a geometrically self-similar tip, another

indentation size effect occurs in the case of a spherical indenter tip. However, the characteristic length of this size effect is the indenter radius itself in a way that the hardness increases as the tip radius decreases [14–18].

Besides the experimental observations, computer simulations have greatly contributed to the investigation of the response of materials during nanoindentation. The common modeling methods are finite element [24–41], crystal plasticity [42–50], discrete dislocation dynamics [51–62], the quasicontinuum method [63–76] and molecular dynamics (MD) [77–88]. Going down from simulations with larger length scales, i.e., finite element, to that of the smallest length scales, i.e., MD, the simulation accuracy increases while the required resources hugely increases. The most accurate method to model the nanoindentation experiment and investigate the underlying physics of the indentation size effect is to model the sample as a cluster of atoms using MD simulation. Accordingly, the MD simulation of nanoindentation can be envisaged as a pseudo-nanoindentation experiment in which the sample is modeled with the accuracy down to the atomic scale.

In the current review, the focus is on the nanoindentation size effect in crystalline metals, in which the deformation mechanisms are governed by the nucleation and evolution of the dislocation network. The size effect trend in which the hardness increases as the indentation depth decreases is considered in the current review. The aim of this study is to address recent advancements in experiments and atomistic simulation to capture the underlying mechanisms of the size effect during nanoindentation. To do so, first, the classical experimental observations and theoretical models of size effects during nanoindentation are reviewed. Next, the interaction of size effects during nanoindentation with the effects of grain size is summarized. The recent advancements for nanoindentation experiments with the focus on various methods of dislocation density measurement are then reviewed. Advanced size effect models, which have been proposed based on the recent experimental observations, are addressed here. Finally, the atomistic simulation of nanoindentation is introduced as a powerful tool to investigate the underlying mechanisms of the size effect during nanoindentation. The dislocation nucleation and evolution pattern observed during the MD simulation of nanoindentation are also summarized. The details and methodology of atomistic simulations, however, are beyond the scope of the current work.

2. Classical Experimental Observations and Theoretical Models

The older generation of size effect observations during indentation have been reported usually as the variation of hardness versus the indentation load (see, e.g., Mott, [5]) during the Vickers microhardness experiment, which has a square-based diamond pyramid. In the early stages of the size effect observations, however, the observed trends have been attributed to the experimental artifacts such as sample surface preparation or indenter tip imperfections. Advancing the nanoindentation techniques and load and depth sensing instruments, however, the obtained results show that the indentation size effects are not artifacts of the experiment, and it has underlying physical mechanisms. Figure 1 shows the common size effect trend for several nanoindentation experiments available in the literature in which the hardness increases as the indentation depth decreases. In Figure 1, for each set of experiments, the hardness is normalized using the hardness value at large indentation depths H_0, at which the hardness becomes independent of the indentation depth. To unravel the governing mechanisms of the size effect during nanoindentation, the concept of geometrically necessary dislocations (GNDs), which was introduced by Ashby [89], has been commonly adopted [11–14,90]. Ashby [89] stated that dislocations could be categorized into two groups. The first one, which is called geometrically necessary dislocations (GNDs), is formed to sustain the imposed displacement for the sake of compatibility. The second type, which is called statistically stored dislocations (SSDs), is a group of dislocations trapping each other in a random way. The model proposed by Nix and Gao [13] is a milestone in this family of models in which they predicted the size effect during nanoindentation using a conical tip (Figure 2). In Figure 2, the SSDs are excluded; however, they contribute to the indentation hardness. During the nanoindentation, the compatibility of deformation between the

sample and indenter is guaranteed by the nucleation and movement of GNDs. Accordingly, the total length of GNDs λ_G can be obtained based on the indentation depth h, contact radius a_p, Burgers vector of GNDs b and indenter geometry as follows (Nix and Gao [13]):

$$\lambda_G = \int_0^{a_p} \frac{2\pi r h}{b a_p} dr = \frac{\pi a_p h}{b} = \frac{\pi a_p^2 \tan(\theta)}{b} \quad (1)$$

where $\tan(\theta) = h/a_p$. In the next step, Nix and Gao [13] assumed that the plastic zone is a hemisphere with the radius of a_p. Accordingly, the density of GNDs ρ_G can be described as follows:

$$\rho_G = \frac{\lambda_G}{V} = \frac{3h}{2ba_p^2} = \frac{3}{2bh} \tan^2(\theta) \quad (2)$$

where V is the volume of the plastic zone.

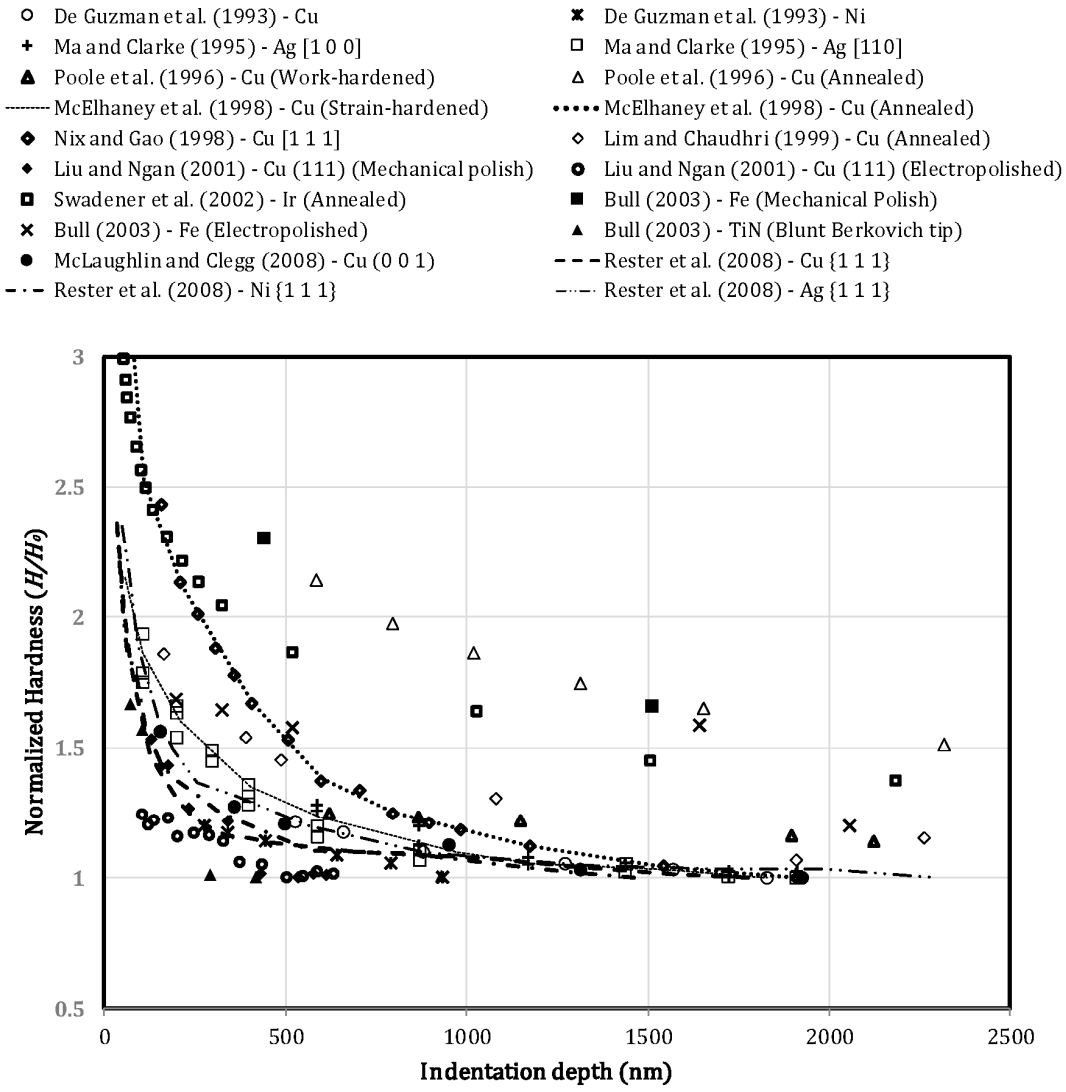

Figure 1. Size effect during nanoindentation. The original experimental data have been reported by De Guzman [12], Ma and Clarke [91], Poole et al. [92], McElhaney et al. [93], Nix and Gao [13], Lim and Chaudhri [15], Liu and Ngan [94], Swadener [14], Bull [20], McLaughlin and Clegg [95] and Rester et al. [96].

Nix and Gao [13] further neglected the interaction between SSDs and GNDs and assumed that the total dislocation density ρ is simply the summation of SSDs and GNDs densities, i.e., $\rho = \rho_S + \rho_G$, where ρ_S and ρ_G are the SSD and GND densities, respectively. Finally, the Taylor hardening model relates the dislocation density ρ to the indentation hardness H as follows [13]:

$$H = 3\sqrt{3}\alpha G b\sqrt{\rho} = 3\sqrt{3}\alpha G b\sqrt{\rho_G + \rho_S} \tag{3}$$

where G is the shear modulus and α is a material constant. Accordingly, the variation of hardness versus the indentation depth can be defined as follows:

$$\frac{H}{H_0} = \sqrt{1 + \frac{h^*}{h}} \tag{4}$$

where H_0 is the hardness due to SSDs and h^* is the characteristic length that governs the dependency of the hardness on the penetration depth. H_0 and h^* can be described as follows:

$$H_0 = 3\sqrt{3}\alpha G b\sqrt{\rho_S} \tag{5}$$

$$h^* = \frac{81}{2} b\alpha^2 \tan^2(\theta)\left(\frac{G}{H_0}\right)^2 \tag{6}$$

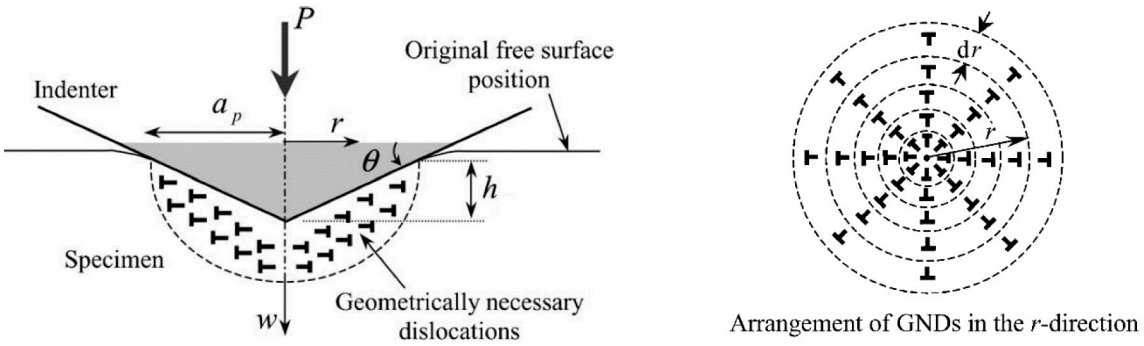

Figure 2. Axisymmetric rigid conical indenter. Geometrically necessary dislocations (GNDs) created during the indentation process. The dislocation structure is idealized as circular dislocation loops (after Abu Al-Rub and Voyiadjis [97]).

In the next step, Nix and Gao [13] connected the physical mechanism of indentation size effect to the strain gradient plasticity model by defining the strain gradient during the nanoindentation as follows:

$$\chi \equiv \frac{\tan(\theta)}{a_p} \tag{7}$$

Accordingly, the length scale for a strain gradient model can be obtained as follows:

$$l \equiv b\left(\frac{G}{\sigma_0}\right)^2 \tag{8}$$

where $\sigma_0 = H_0/3$.

Swadener et al. [14] extended the proposed model of Nix and Gao [13] to include the general indenter geometry of $h = A_r{}^n$, where $n > 1$ and A is a constant. Accordingly, the total dislocation length can be described as follows:

$$\lambda_G = \int_0^{a_p} \frac{2\pi r}{b}\left(\frac{dh}{dr}\right)dr = \frac{2\pi n A}{b(n+1)} a_p^{n+1} \tag{9}$$

Accordingly, the GND density can be described as follows:

$$\rho_G = \frac{\lambda_G}{V} = \frac{3nA}{b(n+1)} a_p^{n-2} = \frac{3nA^{(2/n)}}{b(n+1)} h^{(1-2/n)} \tag{10}$$

Pugno [90] extended the framework proposed by Swadener et al. [14] for the indenter with the general geometry by approximating the indentation surface as a summation of discrete steps due to the formation of dislocation loops (Figure 3). Accordingly, the total GND length can be calculated as follows:

$$\lambda_G = \frac{\Omega - A}{b} = \frac{S}{b} \tag{11}$$

where A and S are the summation of horizontal and vertical surfaces, respectively, and $\Omega = S + A$ (Figure 3). The GND density can be described as follows:

$$\rho_G = \frac{\lambda_G}{V} = \frac{S}{bV} \tag{12}$$

Accordingly, the size effect law can be described based on the surface to volume ratio of the indentation domain.

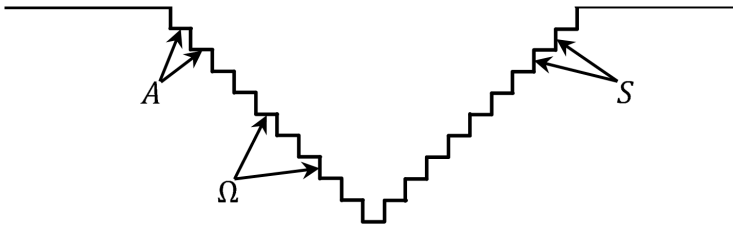

Figure 3. Approximating the indentation surface as a summation of discrete steps: A is the projected contact area; Ω is the contact surface; and $S = \Omega - A$.

Swadener et al. [14] also addressed the size effect during indentation using a spherical tip. The geometry of the spherical tip was approximated by parabola, i.e., $h = r^2/2R_p$. According to Equation (10), $\rho_G = 1/bR_p$, i.e., the density of GNDs is independent of penetration depth for a spherical indenter. However, the size effect for a spherical indenter is governed by another characteristic length, which is the indenter radius R_p. Using the similar methodology as Equation (4), the size effect for spherical indenters can be described as follows:

$$\frac{H}{H_0} = \sqrt{1 + \frac{R^*}{R_p}} \tag{13}$$

where $R^* = \bar{r}/b\rho_S$. Figure 4 compares the theoretical predictions presented by Nix and Gao [13] and Swadener et al. [14]. The results show that the theoretical model can capture the size effects for large indentation depths and indenter radii. In the case of small depths and radii, however, the theoretical models noticeably deviate from the experimental results.

Feng and Nix [98] also showed that the Nix and Gao model [13] cannot capture the size effect in MgO during nanoindentation at lower indentation depths (Figure 5). They investigated three reasons that may induce the Nix and Gao model [13] to break down at small indentation depths: indenter tip bluntness, effect of Peierls stress and dislocation pattern underneath the indenter. They showed that the first two reasons are not responsible for the observed discrepancies. In order to consider the dislocation distribution beneath the indenter, they showed that the modified radius of the plastic zone should be incorporated as follows:

$$R_{pz} = f a_p \tag{14}$$

where f varies as the indentation depth increases. For a large indentation depths, $f \to 1$, the model reduces to the Nix and Gao model [13]. Accordingly, the volume of plastic volume can be obtained as below:

$$V = \frac{2}{3}\pi R_{pz}^3 = \frac{2}{3}\pi f^3 a_p^3 \tag{15}$$

The size effect model based on the modified definition of plastic volume is depicted in Figure 6, which captures the size effect both at large and small indentation depths. Durst et al. [36] incorporated the same method to modify the Nix and Gao model [13]. Instead of variable f, which is fitted using the experiment (Feng and Nix [98]), they proposed that f is a constant. They incorporated $f = 1.9$ in their work and showed that it can capture the size effects in single crystal and ultrafine-grained copper [36].

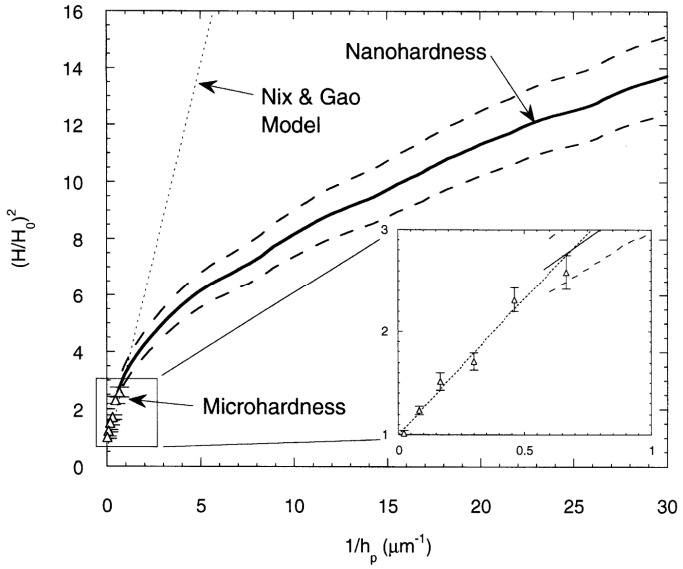

Figure 4. Indentation size effect in annealed iridium measured with a Berkovich indenter (Δ and solid line) and comparison of experiments with the Nix and Gao [13] model ($H_0 = 2.5$ GPa; $h^* = 2.6$ μm). The dashed lines represent ±1 standard deviation of the nanohardness data (after Swadener et al. [14]).

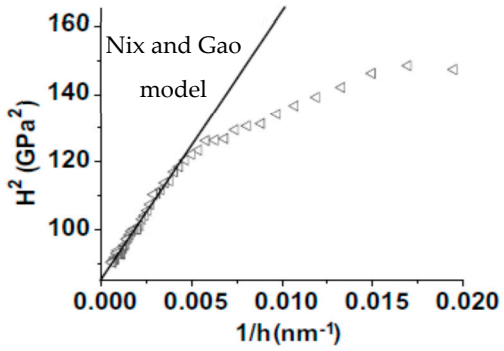

Figure 5. Indentation size effect in polished MgO: experimental results versus the Nix and Gao [13] model ($H_0 = 9.24$ GPa; $h^* = 92.5$ nm) (after Feng and Nix [98]).

In order to modify the Nix and Gao model [13], Huang et al. [99] proposed an analytical model by defining a cap for GND density ρ_G^{max}, which is a material constant. Accordingly, in the case of the conical indenter, the local GND density can be defined as follows:

$$(\rho_G)_{local} = \rho_G^{max} \quad \text{if } h < h_{nano} \tag{16a}$$

$$(\rho_G)_{\text{local}} = \begin{cases} \rho_G^{\max} & \text{for} \quad r < \frac{h_{\text{nano}}}{\tan(\theta)} \\ \frac{\tan(\theta)}{br} & \text{for} \quad \frac{h_{\text{nano}}}{\tan(\theta)} \leq r \leq a_p = \frac{h}{\tan(\theta)} \end{cases} \tag{16b}$$

where $h_{\text{nano}} = \tan^2(\theta)/\left(b\rho_G^{\max}\right)$ is a nanoindentation characteristic length. The average GND density can be obtained by averaging $(\rho_G)_{\text{local}}$ over the plastic zone volume, which is a hemisphere with the radius of a_p, as follows [99]:

$$\rho_G = \rho_G^{\max} \begin{cases} 1 & \text{if } h < h_{\text{nano}} \\ \frac{3h_{\text{nano}}}{2h} - \frac{h_{nano}^3}{2h^3} & \text{if } h < h_{\text{nano}} \end{cases} \tag{17}$$

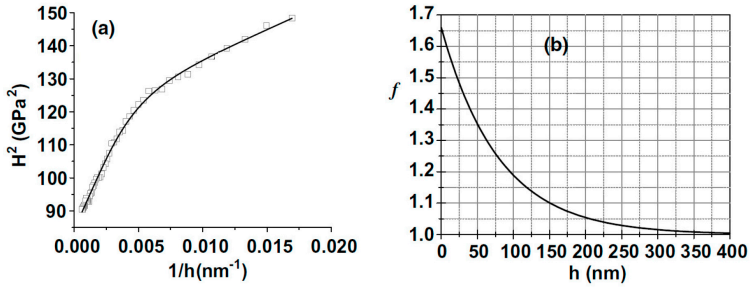

Figure 6. Indentation size effect in polished MgO: (**a**) experimental results versus the modified Nix and Gao model presented by Feng and Nix [98] ($H_0 = 9.19$ GPa; $h^* = 102$ nm); (**b**) variation of f versus h (after Feng and Nix [98]).

Based on the modified GND density, Huang et al. [99] developed a strain gradient plasticity model and captured the indentation size effect in MgO and Ir (Figure 7). The values of $\rho_G^{\max}$ for MgO and Ir are 1.28×10^{16} m^{-2} and 9.68×10^{14} m^{-2}, respectively.

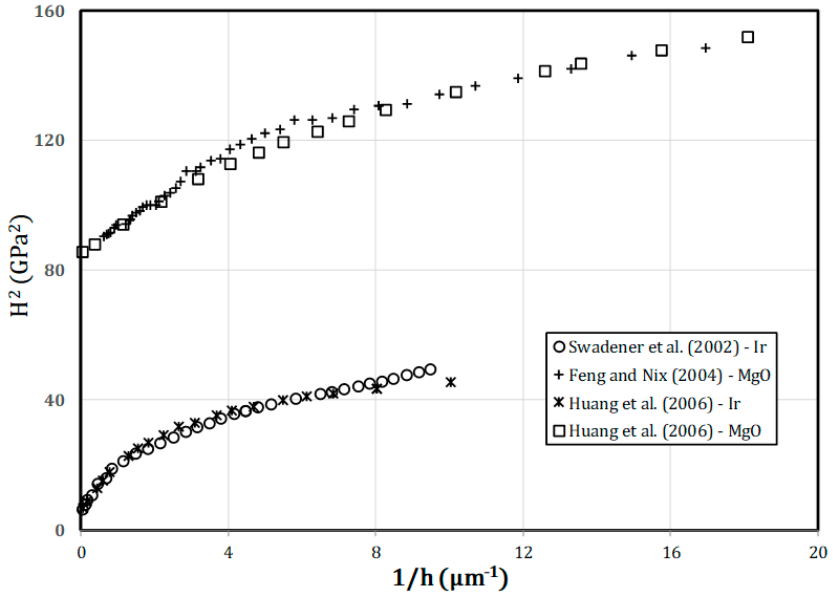

Figure 7. Comparison between the indentation size effect captured using the strain gradient plasticity model developed by Huang et al. [99] using a cap for GND density versus the experimental results in Ir and MgO ($\rho_G^{\max}{}_{\text{Ir}} = 9.68 \times 10^{14}$ m^{-2}, $\rho_G^{\max}{}_{\text{MgO}} = 1.28 \times 10^{16}$ m^{-2}). The original simulation and experimental data have been reported by Swadener [14], Feng and Nix [98] and Huang et al. [99].

3. Interaction of Size Effects during Nanoindentation and Grain Size Effects

The interaction between the effects of grain size with indentation size effects have been addressed both theoretically and experimentally [100–108]. Here, the experimental and theoretical studies conducted by Voyiadjis and his coworkers [103–108] are discussed in more detail. Figure 8 compares the response of single crystalline and polycrystalline Al during nanoindentation. In the case of single crystalline Al, the conventional size effects trend can be observed. In the case of polycrystalline Al, however, a local hardening can be observed, which is due to the effect of the grain boundary (GB). In order to capture the effect of GB, the theoretical model has been proposed by Voyiadjis and his coworkers [103–108] based on the concept of GNDs and the methodology developed by Nix and Gao [13]. Figure 9 depicts the effect of GB on the dislocation movement pattern during nanoindentation. Unlike the single crystalline metals, the GNDs movements are blocked by grain boundaries, which induce a dislocation pile-up against the GB. Accordingly, a local hardening is induced in the nanoindentation response due to the GB resistance. The dislocation can move to the next grain when the stress concentration induced by dislocation pile-up reaches a critical value, and the nanoindentation response follows the conventional size effect pattern. Accordingly, the schematic of effects of GB on the nanoindentation response can be divided into three regions (Figure 10). In Region I, the indenter does not feel the GB, and the initial nucleation and evolution of GNDs govern the size effect, which is similar to the response of a single crystal sample. Eventually, the dislocations reach the GB at which their movements are blocked, and they pile-up against the GB, which leads to a local hardening (Region II). The pile-up stress eventually reaches a critical value, and dislocations will dissociate to the next grain; additionally, the nanoindentation response follows that of a single crystal sample (Region III).

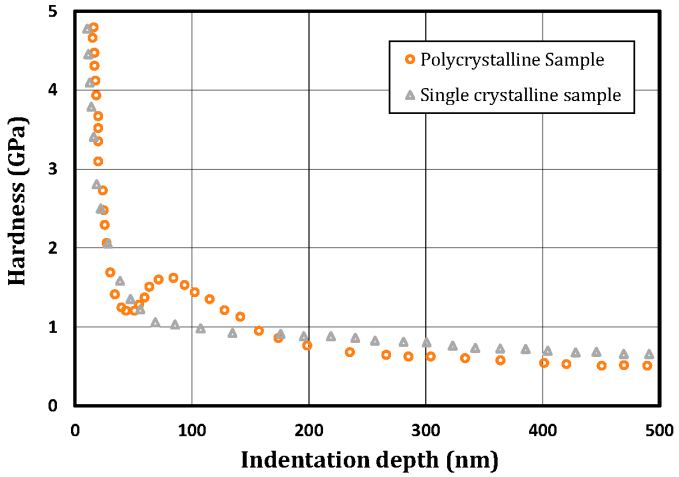

Figure 8. Comparison of the nanoindentation response of a single crystalline Al sample with that of a polycrystalline one at strain rates of 0.1 s^{-1}. The original data were reported by Voyiadjis et al. [106].

Voyiadjis and Zhang [107] and Zhang and Voyiadjis [108] investigated the effects of GB on the nanoindentation response of bicrystalline Al and Cu samples, respectively. They varied the distance of indentation from the GB and compared the observed nanoindentation responses (Figure 11). The results showed that the distance from the GB controls the depths at which different regions of hardening occur in a way that the local hardening occurs at lower indentation depths for indentations closer to the GB. As the indentation distance becomes large enough, the response becomes similar to that of a single crystalline sample. Accordingly, Zhang and Voyiadjis [108] proposed a material length scale that incorporates the effect of distance between the GB and indenter tip r based on the framework

developed by Nix and Gao [13], Abu Al-Rub and Voyiadjis [97], Voyiadjis and Abu Al-Rub [109] and Voyiadjis et al. [106] as follows:

$$l = \left(\frac{\alpha_G}{\alpha_S}\right)^2 \left(\frac{b_G}{b_S}\right) \overline{M} r \left\{ \frac{\delta_1 r e^{-(E_r/RT)}}{\left[1 + \delta_2 r p^{(1/\tilde{m})}\right]\left[1 + \delta_3 (\dot{p})^q\right]} \right\} \tag{18}$$

where d_g is the average grain size, $\overline{M}$ is the Schmid factor, $1/\tilde{m}$ and q are the hardening exponents, δ_1, δ_2 and δ_3 are the material constants calibrated using the nanoindentation experiment, E_r is the activation energy, R is the gas constant and T is the absolute temperature.

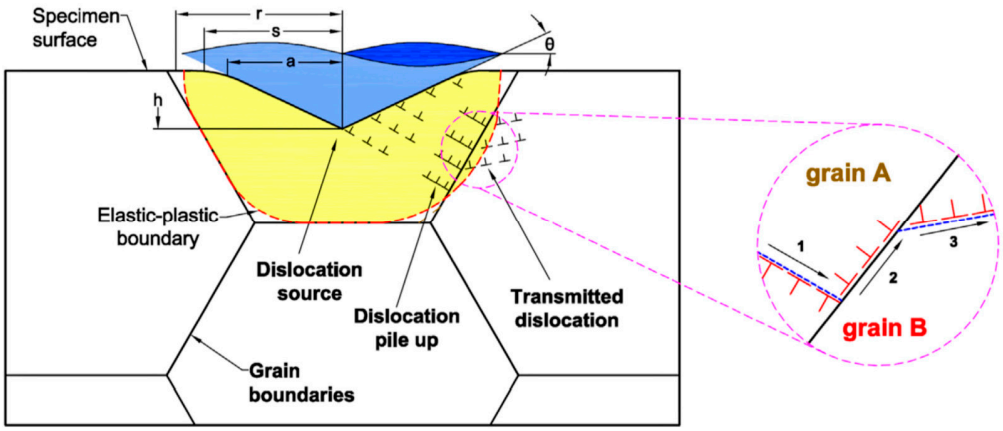

Figure 9. The schematic of the interaction between the GNDs and grain boundaries for polycrystalline metals during nanoindentation (after Voyiadjis and Zhang [107]).

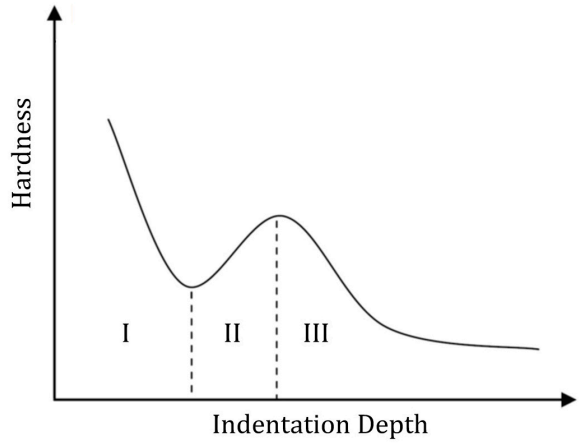

Figure 10. The typical nanoindentation response of polycrystalline samples.

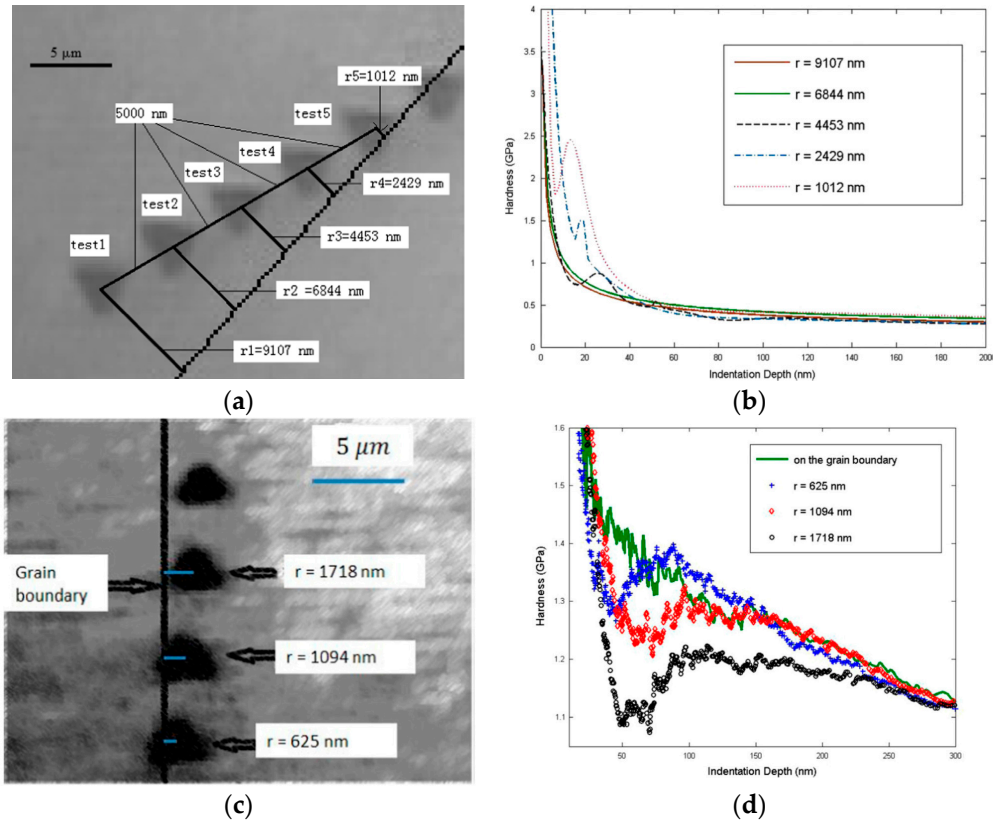

Figure 11. Effect of grain boundary on the nanoindentation response of crystalline metals: (**a**) distances between the grain boundary and indentations for Al bicrystal sample; (**b**) the effect of the distance from indentation to the grain boundary on the nanoindentation response of the Al bicrystal sample; (**c**) distances between the grain boundary and indentations for the Cu bicrystal sample; (**d**) the effect of the distance from indentation to the grain boundary on the nanoindentation response of the Cu bicrystal sample (after Voyiadjis and Zhang [107] and Zhang and Voyiadjis [108]).

4. Recent Experimental Observations and Theoretical Models

The fundamental assumption in the size effects model based on the density of GNDs following the Nix and Gao model [13] is that the forest hardening is the governing mechanism. Accordingly, they relate the size effect to the GNDs induced by the strain gradient, which enhances the nanoindentation response. As described by Swadener et al. [14], Feng and Nix [98] and Huang et al. [99], the Nix and Gao model [13] cannot capture the size effects at shallow indentation depths. Although different methods of modifying the plastic zone volume [98] and assigning a GND saturation cap [99] solved the model shortcomings to some extent, both methods are phenomenological in nature, and they are using fitting procedures to solve the problem. Furthermore, these models still incorporate the forest hardening mechanism to capture the relation between the material strength and dislocation density.

Uchic and his coworkers [110,111] introduced the micropillar compression experiment and showed that the crystalline metallic samples show strong size effects even in the absence of any strain gradients. They have tested pure Ni pillars at room temperature and showed that the sample strength increases by decreasing the pillar diameter (Figure 12). In order to capture the size effect in pillars, however, other hardening mechanisms, including source truncation, weakest link theory and source exhaustion, have been introduced rather than the forest hardening mechanism (see, e.g., Uchic et al. [112] and Kraft et al. [113]) In micropillars, the double-ended dislocation sources become single-ended ones due to the interaction of dislocations with the pillar-free surfaces. Accordingly, the pillar size governs the single-ended sources leading to shorter dislocation sources

for smaller pillars. Consequently, decreasing the pillar size increases the sample strength, which is commonly called the source truncation mechanism (Parthasarathy et al. [114]; Rao et al. [115]). Another hardening mechanism is the weakest link theory (Norfleet et al. [116]), which describes that decreasing the pillar size increases the strength of the weakest deformation mechanism and leads to the increase in the sample strength. The third hardening mechanism is source exhaustion (see, e.g., Rao et al. [117]), which states that the material strength increases when not enough dislocation sources are available to sustain the applied plastic flow. In the case of pillars, dislocation starvation (Greer et al. [118]) is one of the mechanism that can lead to the source exhaustion in a way that all the dislocations escape from the pillar-free surfaces, leaving the sample without any dislocations. Accordingly, the sample strength is controlled by source-limited activations.

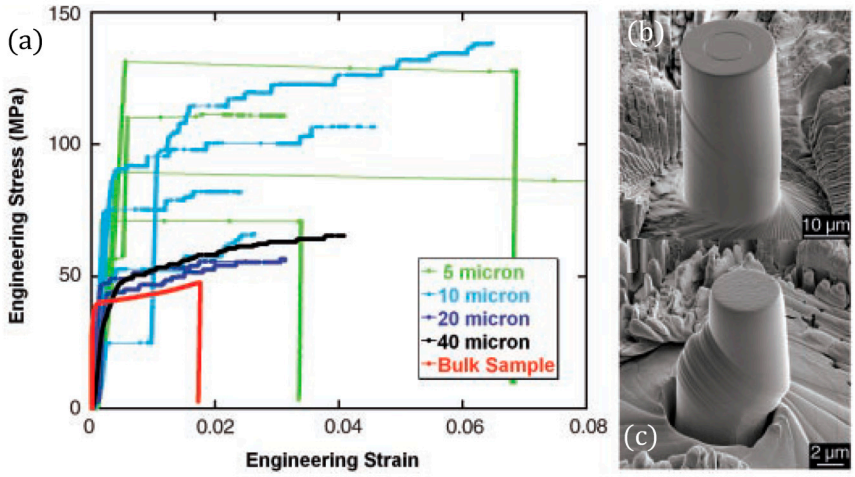

Figure 12. Response of pure Ni pillars during the uniaxial compression experiment at room temperature. (**a**) Stress-strain curves for pillars with diameters that vary from 40 to 5 μm and a bulk single crystal having approximate dimensions of 2.6 × 2.6 × 7.4 mm; (**b**) A scanning electron micrograph (SEM) image of a pillar with the diameter of 20 μm at 4% strain; (**c**) A SEM image of 5 μm diameter pillar at 19% strain during a rapid burst of deformation (after Uchic et al. [111]).

In order to unravel the hardening mechanism at small indentation depths, the dislocation microstructure should be monitored. Three experimental techniques of backscattered electron diffraction (EBSD) [22,43,45,49,50,96,119–121], convergent beam electron diffraction (CBED) [95] and X-ray microdiffraction (μXRD) [122–125] have been used so far to observe the dislocation microstructure in metallic samples. These techniques can map the local lattice orientations with high spatial resolutions. Accordingly, the Nye dislocation density tensor and the associated GND density can be calculated. Due to the complex nature of these experimental schemes, the number of works addressing the size effects during nanoindentation is very limited. Kiener et al. [119], McLaughlin and Clegg [95] and Demir et al. [121] have reported anomalies regarding the description based on the forest hardening mechanism and strain gradient theory to capture the size effects during nanoindentation. Kiener et al. [119] indented the tungsten and copper samples using a Vickers indenter and used EBSD to quantify the lattice misorientation. They incorporated the misorientation angle as a represented parameter of GND density. They showed that the maximum misorientation angle ω_f increases as the indentation depth increases, while the nanoindentation hardness decreases (Figure 13), which cannot be described based on the strain gradient theory and forest hardening mechanism. McLaughlin and Clegg [95] investigated the size effects in a copper single crystal sample indented by a Berkovich tip using CBED. They measured the total misorientation for two indentation loads of 5 mN and 15 mN. It was observed that both the magnitude of the overall misorientation and the neighbor-to-neighbor misorientations underneath the 15 mN indentation are significantly larger than

underneath the 5 mN indentation. However, the hardness for indentation load of 5 mN is larger than that of 15 mN. Again, McLaughlin and Clegg [95] showed that the models based on the strain gradient theory and forest hardening mechanisms, such as Nix and Gao [13], are not applicable to the shallow indentations. They attributed the observed size effects to the lack of dislocation sources at lower indentation loads, which is similar to the source exhaustion mechanism.

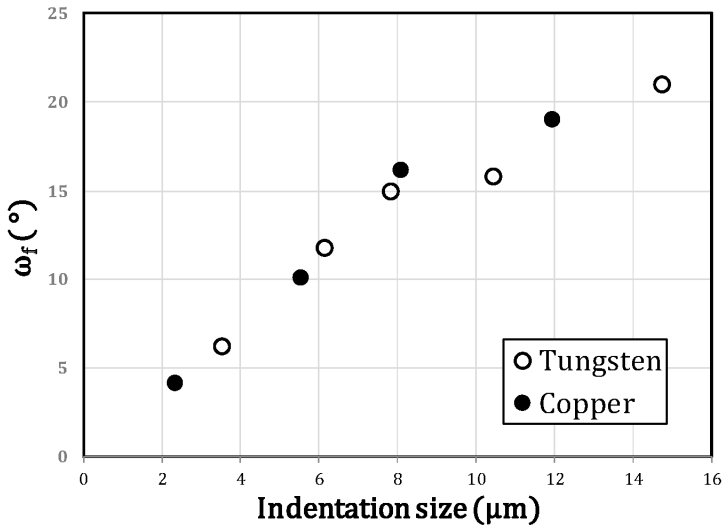

Figure 13. Variation of the maximum misorientation angle ω_f versus the indentation size in tungsten and copper. The original data were reported by Kiener et al. [119].

Demir et al. [121] investigated the size effects at low indentation depths incorporating the GND density obtained using EBSD tomography. They conducted the nanoindentation test on a single crystal Cu sample using a conical indenter with a spherical tip. Figure 14 illustrates the GND density pattern for five equally-spaced cross-sections at four different indentation depths. The results show that the assumption that the dislocations are homogenously distributed beneath the indenter, which has been commonly incorporated in the literature, is not accurate. Furthermore, Demir et al. [121] obtained the total dislocation density using the information obtained from 50 individual 2D EBSD sections at different indentation depths. Figure 15 shows the variation of both dislocation density and hardness as the indentation depth varies. As the results show, the density of GNDs increases as the indentation depth increases. According to the forest hardening mechanisms and consequently the Nix and Gao model [13], the hardness should also increase. However, as the results show, the hardness decreases as the indentation depth increases. This means that the forest hardening mechanism breaks down at shallow indentation depths, and the models developed based on the premise, i.e., Nix and Gao model [13] and its relating models, are not valid in this region. Demir et al. [121] attributed the observed hardening to the decreasing dislocation segment lengths as the indentation depth decreases, which has a similar nature to the source truncation and weakest link theory mechanisms. One should note that the conducted experiments solely consider the GNDs and not SSDs. Accordingly, the result may not be dependable. However, Demir et al. [121] stated that the amount of imposed deformation decreases by decreasing the indentation depth, and consequently, SSDs are not responsible for the enhanced hardening at lower indentation depths.

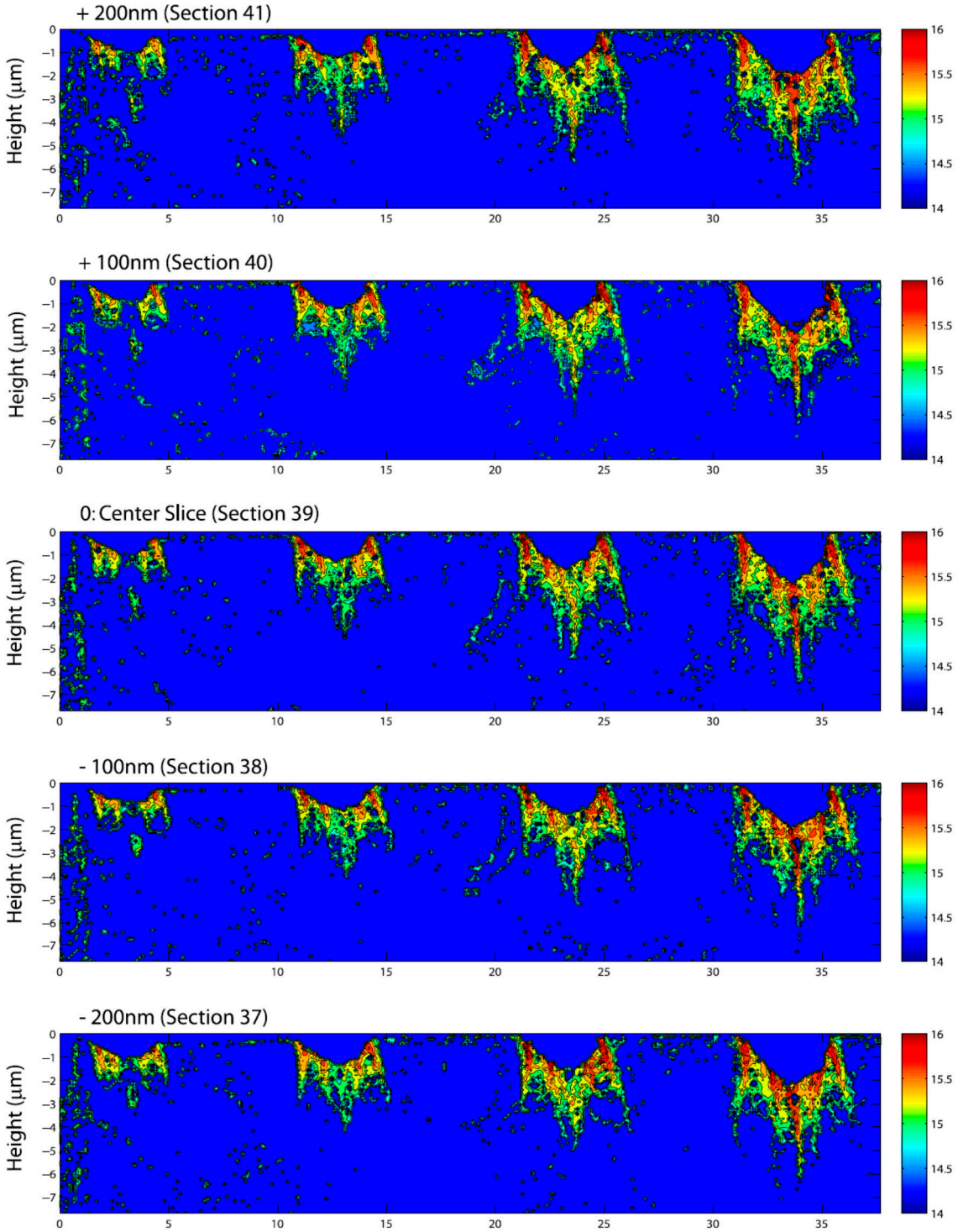

Figure 14. Five equally-spaced cross-sections (center slice, ±100 nm, ±200 nm) through the four indents. Color code: GND density in decadic logarithmic scale (m^{-2}) (after Demir et al. [121]).

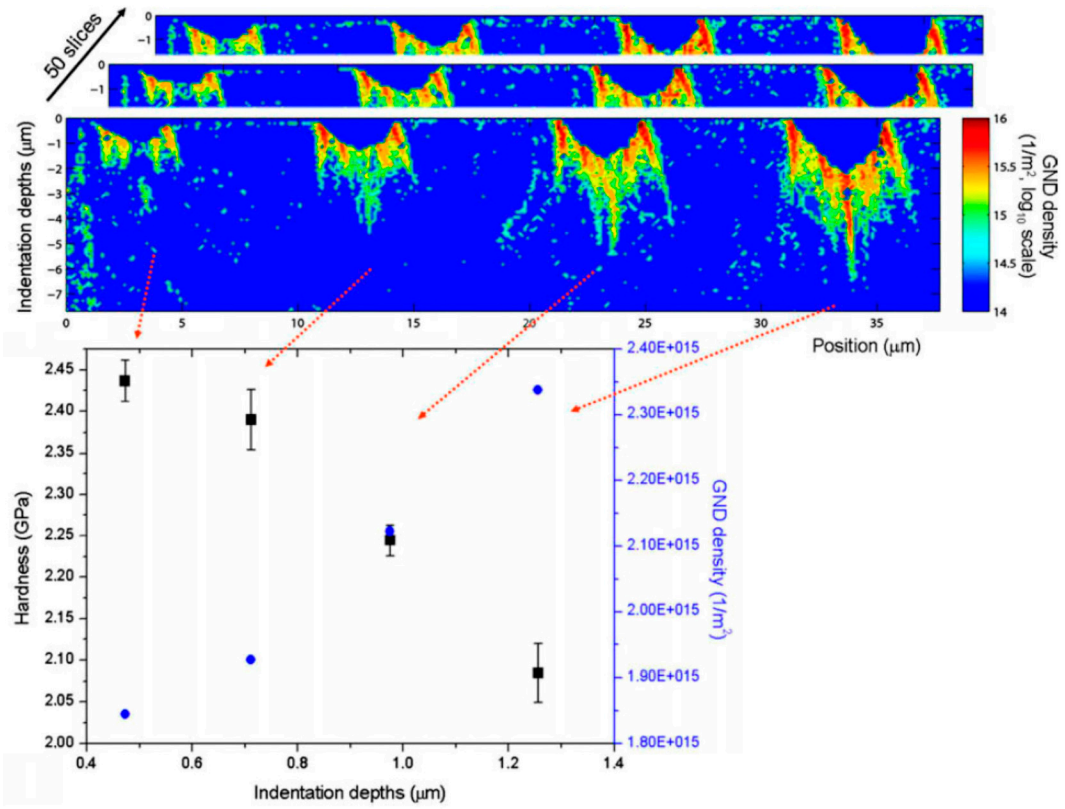

Figure 15. The variations of hardness and GND density versus the indentation depth (after Demir et al. [121]).

Feng et al. [125] incorporated the μXRD scheme and studied the evolution of defects in Cu single crystal during nanoindentation indented using a Berkovich indenter. Feng et al. [125] stated that the size effects are in line with the strain gradient theory and forest hardening mechanism even at shallow indentation depths, which is in contradiction with the results reported by Kiener et al. [119], McLaughlin and Clegg [95] and Demir et al. [121]. They observed that as the indentation depth decreases, both GND density and hardness increases. However, unlike Demir et al. [121], which obtained the GND density pattern below the indenter, Feng et al. [125] approximated the strain gradient. Accordingly, the equation of total GND density depends on the radius of the plastic zone, which was assumed to be the contact radius multiplied by a constant. Accordingly, the effect of heterogeneity reported by Demir et al. [121] was not included in the methodology presented by Feng et al. [125] to obtain the total GND density. In order to investigate whether the trend reported by Kiener et al. [119], McLaughlin and Clegg [95] and Demir et al. [121] is accurate or the one presented by Feng et al. [125], the meso-scale simulations, such as the atomistic simulation, should be incorporated.

5. Atomistic Simulation of Nanoindentation

The microstructural observations during the nanoindentation indicate some contradictions in a way that both the increase and decrease in GND density have been reported as the indentation depths decrease [95,119,121,125]. In order to shed light on these discrepancies and unravel the governing mechanism of size effects during nanoindentation, one way is to model the sample as a cluster of atoms. Molecular dynamics (MD) is a powerful tool that can be incorporated as a pseudo-experimental tool to address the size effect during the nanoindentation. In the case of crystalline metals, many different aspects of nanoindentation experiment, such as initial dislocation nucleation and evolution pattern [79,81,83], the effect of surface step [80], effects of GB [84,88,126,127], the effect of film thickness [128], the effect of substrate [129], the effect of residual stress [130], the effect

of boundary conditions [85] and size effects during nanoindentation [86,87] have been investigated using MD. Szlufarska [131] summarized the advances in atomistic modelling of the nanoindentation experiment. She addressed the challenges of atomistic simulation of nanoindentation and how it can increase the current understanding of nanoindentation [131].

During the MD simulation, Newton's equations of motion are solved for all the atoms. Even for nano-sized samples, the number of degrees of freedom is enormous, and massive parallel code should be incorporated to integrate Newton's equations of motion. The interaction of atoms with each other is described using predefined potentials. In the case of crystalline metals, two potentials of the embedded-atom method (EAM) (Daw and Baskes [132]) and modified embedded-atom method (MEAM) (Baskes [133]) are commonly incorporated.

The indenter itself can be modeled as a cluster of atoms. However, the indenter is commonly modeled as a repulsive potential to reduce the computational cost. Selecting an appropriate set of boundary conditions to precisely mimic the considered phenomenon is an essential part of the MD simulation. Up to now, four different sets of boundary conditions have been used to model the nanoindentation experiment, which can be described as follows:

- Fixing some atomic layers at the sample bottom to act as a substrate, using the free surface for the top and periodic boundary conditions for the remaining surfaces (see, e.g., Kelchner et al. [79]; Zimmerman et al. [80]; Nair et al. [128]).
- Fixing some atomic layer at the surrounding surfaces and using free surfaces for the sample top and bottom (see, e.g., Medyanik and Shao [134]; Shao and Medyanik [135]).
- Using the free surface for the sample top and bottom, incorporating the periodic boundary conditions for the remaining surfaces and putting a substrate under the thin film (see, e.g., Peng et al. [129]).
- Incorporating the free surfaces for the sample top and bottom, using periodic boundary conditions for the remaining surfaces and equilibrating the sample by adding some forces (see, e.g., Li et al. [81]; Lee et al. [83]).

Yaghoobi and Voyiadjis [85] studied the effects of selected boundary conditions on the nanoindentation response of FCC crystalline metals. They showed that the boundary conditions may alter the plasticity initiation and defect nucleation pattern depending on the film thickness and indenter radius.

In order to study the size effects using MD, indentation depth, indentation force, contact area and dislocation length and density should be precisely obtained. In the case of hardness, unlike the experiment, the precise contact can be obtained much more easily. To do so, the precise contact area (A) should be captured to calculate the hardness. Saraev and Miller [136] proposed a method using a projection of atoms that are in contact with the indenter to obtain the precise contact area. A 2D-mesh is produced from the projections of atoms in contact with the indenter. The total contact area is then calculated using the obtained 2D mesh. The indenter force can be derived from the repulsive potential used to model the indenter. Voyiadjis and his co-workers [85–87] showed that the true indentation depth h is different from the tip displacement d during nanoindentation. They developed the required geometrical equations to obtain the precise indentation depth.

MD provides the atomic trajectories and velocities. However, the dislocation structure is an essential part of the size effects' investigation. Accordingly, a post-processing scheme should be incorporated to capture the dislocation structure. In order to visualize the defects, several methods have been introduced such as energy filtering, bond order, centrosymmetry parameter, adaptive common neighbor analysis, Voronoi analysis, and neighbor distance analysis, which have been compared with each other by Stukowski [137]. Furthermore, the Crystal Analysis Tool (Stukowski and Albe [138]) can extract the dislocation structure from the atomistic data. The common-neighbor analysis method is the basic idea of this code. The code is able to calculate the dislocations information such as the Burgers vector and total dislocation length. To extract the required information, the Crystal

Analysis Tool constructs a Delaunay mesh, which connects all atoms. Next, using the constructed mesh, the elastic deformation gradient tensor is obtained. The code defines the dislocations using the fact that the elastic deformation gradient does not have a unique value when a tessellation element intersects a dislocation.

Voyiadjis and Yaghoobi [86] conducted large-scale MD simulation of Ni thin film during nanoindentation using different indenter geometries of right square prismatic, conical and cylindrical to investigate the proposed theoretical models for indentation size effects. First, Voyiadjis and Yaghoobi [86] investigated the dislocation nucleation and evolution pattern during nanoindentation. As an example, Figure 16 shows the dislocation nucleation and evolution for Ni thin film indented by a cylindrical indenter during nanoindentation. The dislocations and stacking faults are visualized while the perfect atoms are removed. The color of Shockley, Hirth and stair-rod partial dislocations and perfect dislocations are green, yellow, blue and red, respectively. Figure 17 illustrates the dislocation loop formation and movement along three directions of $[\bar{1}\ 0\ \bar{1}]$, $[\bar{1}\ \bar{1}\ 0]$ and $[0\ \bar{1}\ \bar{1}]$.

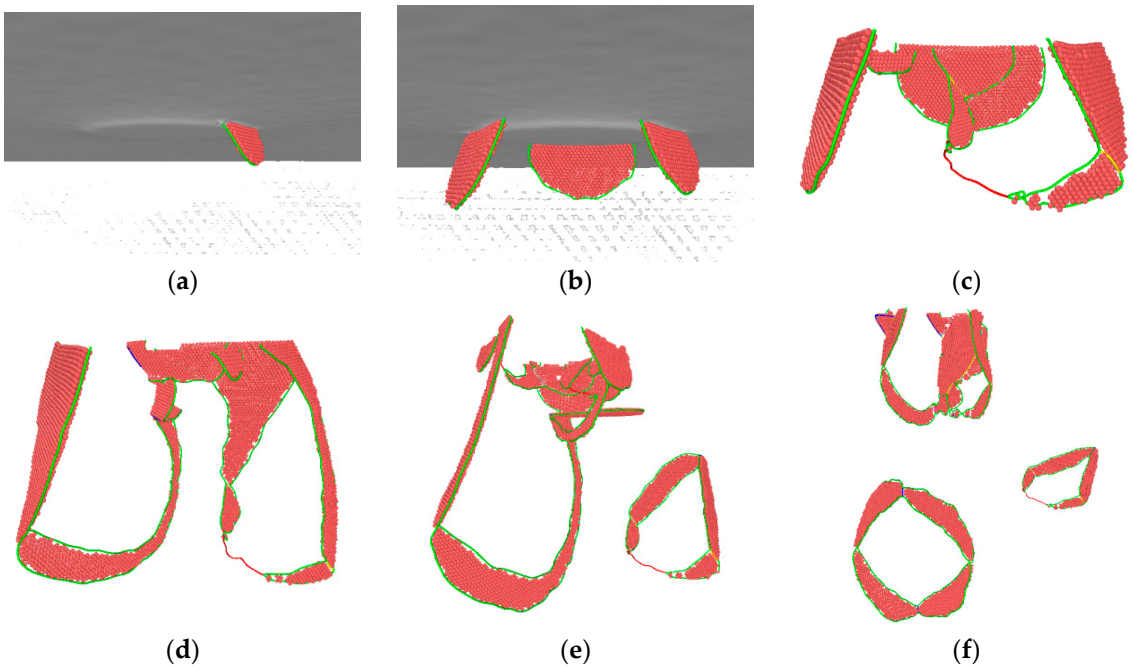

Figure 16. Defect nucleation and evolution of Ni thin film indented by a cylindrical indenter at different indenter tip displacements of (**a**) $d \approx 0.70$ nm; (**b**) $d \approx 0.86$ nm; (**c**) $d \approx 0.96$ nm; (**d**) $d \approx 1.02$ nm; (**e**) $d \approx 1.05$ nm; (**f**) $d \approx 1.12$ nm (after Voyiadjis and Yaghoobi [86]).

Voyiadjis and Yaghoobi [86] investigated the plastic zone size measured directly from MD. The dislocation prismatic loops glide toward the bottom of the sample. Accordingly, Voyiadjis and Yaghoobi [86] assumed that theses dislocation loops should not be considered as a measure of the plastic zone size. Otherwise, the size of the plastic zone becomes unreasonably large. In other words, the plastic zone size is determined based on the furthest dislocation that is attached to the main body of dislocations beneath the indenter. It was assumed that the plastic zone is a hemisphere with a radius of $R_{pz} = fa_c$. They showed that f is a function of indentation depth. In the case of the conical indenter, which is a self-similar indenter, the maximum value of f observed during the nanoindentation simulation is 5.2, which is larger than those that have been previously proposed (see Durst et al. [36]). However, in the case of cylindrical indenter, the maximum value of f is nine, which is much larger than that of the self-similar indenter.

Figure 18 compares the dislocation lengths obtained from atomistic simulation with those predicted by theoretical models of Nix and Gao [13], Swadener [14] and Pugno [90]. The results show

that the theoretical predictions can accurately capture the dislocation lengths during nanoindentation. However, some discrepancies are observed, which can be related to the fact that atomistic simulation captures the total dislocation length including both geometrically necessary and statistically stored dislocations, while the theoretical models only calculate geometrically necessary dislocations. Furthermore, the dislocations that are detached from the main dislocations network as the prismatic loops and leave the plastic zone around the indenter are not considered in the total dislocation length calculations. Gao et al. [139] investigated the plastic zone volume size during the nanoindentation in FCC and BCC metals using a spherical indenter. They showed that the plastic zone size is not strongly influenced by the crystallographic orientation, crystal structure and the selected parameter for indentation. Furthermore, they observed that the plastic zone sizes after indent are larger than the values reported in the literature. These findings are in line with those reported by Voyiadjis and Yaghoobi [86]. However, they showed that after the indenter retraction, the plastic zone shrinks, and its size becomes closer with those reported in the literature (see Durst et al. [36]). Figure 19 shows the plastic zone volume changes after indent and after retraction during nanoindentation of Ta. The plastic zone coefficient f changes from 2.7 to 2.3.

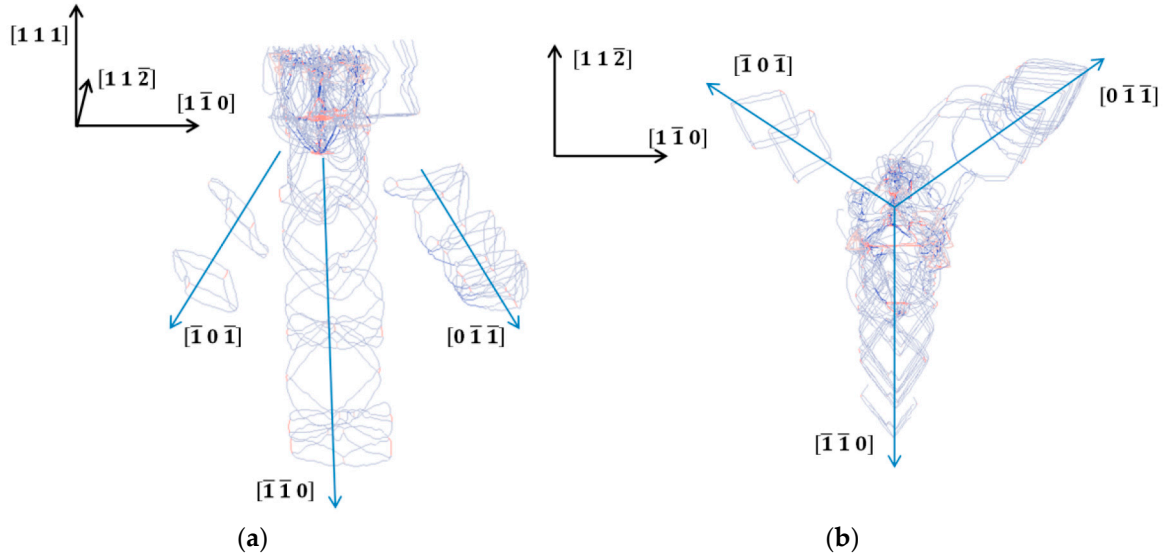

Figure 17. Prismatic loops forming and movement in Ni thin film indented by the cylindrical indenter during nanoindentation: (**a**) side view and (**b**) top view (after Voyiadjis and Yaghoobi [86]).

Yaghoobi and Voyiadjis [87] incorporated large-scale MD simulation of Ni thin films during nanoindentation to investigate which size effect trend occurs during atomistic simulation, i.e., the one reported by Kiener et al. [119], McLaughlin and Clegg [95] and Demir et al. [121] or the one presented by Feng et al. [125]. They selected a conical indenter with an angle of $\theta = 60^{\circ}$ and a spherical tip, which was used by Demir et al. [121]. Figure 20a presents the variation of the mean contact pressure $(p_m = P/A)$, which is equivalent to the hardness H in the plastic region, as a function of indentation depth h. In the elastic region, Figure 20a shows that p_m increases as the indentation depth increases. However, after the initiation of plasticity, Figure 20a shows that the mean contact pressure, i.e., hardness, decreases as the indentation depth increases. Yaghoobi and Voyiadjis [87] assumed that the plastic zone is a hemisphere with the radius of $R_{\mathrm{pz}} = fa_c$ in which f is a constant. They incorporated different values of $f = 1.5,\ 2.0,\ 2.5,\ 3.0$ and 3.5, which are chosen to investigate the effect of plastic zone size on the dislocation density during nanoindentation. The dislocation density ρ versus the indentation depth h is plotted in Figure 20b. The results indicate that as the indentation depth increases, the dislocation density also increases for different values of f. Based on the Taylor hardening model, since the dislocation density increases as the indentation depth increases,

the hardness should also increase. However, Figure 20a shows that as the indentation depth increases, the hardness decreases, while the dislocation density increases. The observed trend is in line with the experimental observation of Kiener et al. [119], McLaughlin and Clegg [95] and Demir et al. [121]. In other words, the results show that the forest hardening model cannot capture the size effect in the case of the simulated sample.

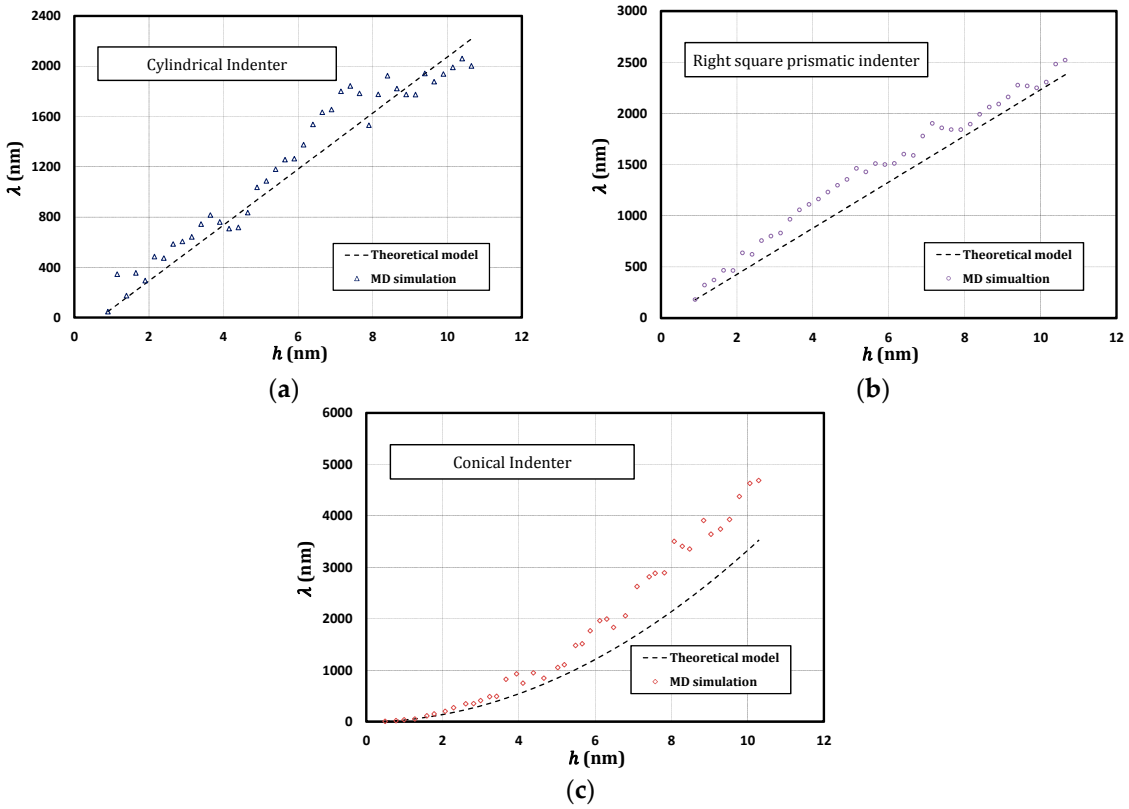

Figure 18. Total dislocation length obtained from the simulation and theoretical models of Nix and Gao [13], Swadener [14] and Pugno [90] in samples indented by the (**a**) cylindrical indenter; (**b**) right square prismatic indenter and (**c**) conical indenter (after Voyiadjis and Yaghoobi [86]).

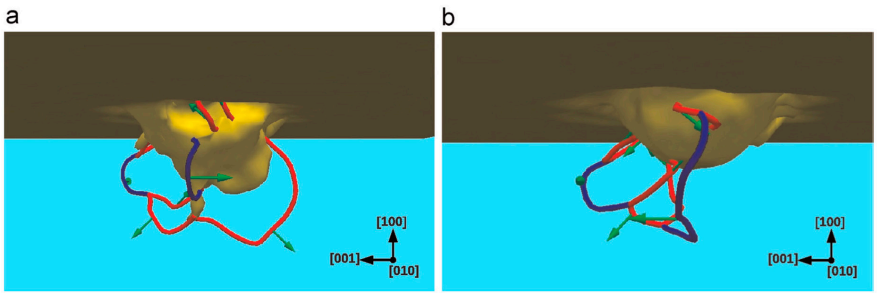

Figure 19. Dislocation structure beneath the indenter during the indentation of Ta (100) surface at 0 K: (**a**) after indent $f = 2.7$; (**b**) after retraction of the indenter $f = 2.3$ (after Gao et al. [139]).

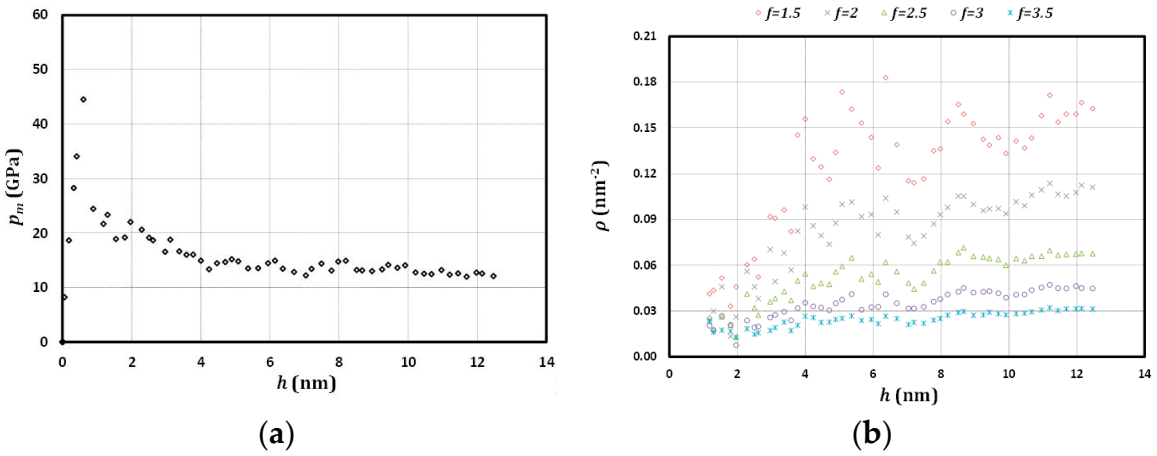

Figure 20. Large-scale atomistic simulation of a Ni thin film during nanoindentation: (**a**) variation of the mean contact pressure p_m versus the indentation depth h; (**b**) variation of the dislocation density ρ versus the indentation depth h for different values of f (after Yaghoobi and Voyiadjis [87]).

Similar to the compression and tension experiments on micropillars of small length scales, the observed results show that the forest hardening mechanism does not govern size effects in the nanoscale samples during nanoindentation. To unravel the sources of size effects, the initial phases of indentation should be studied. Yaghoobi and Voyiadjis [87] showed that the source exhaustion hardening is the governing mechanism of size effects at shallow indentation depths. By increasing the indentation depth, the dislocation length and density increase, as well, which provides more dislocation sources. Furthermore, the source lengths increase, which reduces the critical resolved shear stress. Consequently, the applied stress required to sustain flow during nanoindentation decreases, i.e., hardness decreases as indentation depth increases.

The interaction between the effects of grain size with indentation size effects have been addressed using MD [84,88,126,127]. However, the observed trends do not show a unified trend. Jang and Farkas [84] incorporated MD simulation and studied a bicrystal nickel thin film with $\sum 5\ (2\ 1\ 0)\ [0\ 0\ 1]$ GB during the nanoindentation. It was shown that the GB induced some resistance to the indentation due to the stacking fault expansion [84]. Kulkarni et al. [127] compared the response of the coherent twin boundary (CTB) with that of $\sum 9\ (2\ 2\ 1)$ tilt GB during nanoindentation using atomistic simulation. They stated that unlike the $\sum 9\ (2\ 2\ 1)$ GB, the CTB does not considerably reduce the strength of the sample. However, unlike Jang and Farkas [84], they did not observe noticeable enhancement in strength. In order to address the discrepancies observed related to the effect of grain boundaries on the indentation response of FCC metals during nanoindentation, Voyiadjis and Yaghoobi [88] investigated the nanoindentation response of bicrystal Ni samples using large-scale MD simulation. They incorporated different symmetric and unsymmetric CSL GBs and two large and small samples with the dimensions of 24 nm × 24 nm × 12 nm and 120 nm × 120 nm × 60 nm. The GBs are located at a third of the thickness from the top surface. Voyiadjis and Yaghoobi [88] compared the nanoindentation response of the bicrystal samples with the corresponding single crystal ones and observed that the effect of GB on the governing mechanism of hardening depends on the grain size. Figure 21 compares the effects of $\sum 11\ (3\ 3\ 2)\ [1\ \bar{1}\ 0]$ on the nanoindentation responses of the small and large samples. GB does not change the general pattern of size effects; however, it can contribute to some specific mechanisms depending on the sample size. The size effects are initially controlled by the source exhaustion mechanism during the nanoindentation. In the case of a small sample, Voyiadjis and Yaghoobi [88] showed that the GB contributes to the dislocation nucleation and reduces the material strength. In the case of a large sample, GB does not have any noticeable effect on the source exhaustion mechanism. This is due to the fact that the total dislocation length of the bicrystal sample is close to that of the single crystal sample. The forest hardening mechanism becomes dominant at larger indentation

depths. In the cases of small samples, however, the responses of bicrystal and single-crystal samples are similar in this region. It is worth mentioning that the dislocation movements are blocked by GBs during nanoindentation in small bicrystal samples. However, the density of piled-up dislocation is not enough to change the nanoindentation response. In the cases of large samples, the total dislocation content is much greater than that of the small samples. Accordingly, the interaction of dislocations and GBs plays a key role. Hence, the increase in bicrystal samples can be justified by blockage of the dislocation movements according to the forest hardening mechanism. Moreover, the results show that the total dislocation length in the upper grain is a better representative factor to investigate the strength size effects in the case of the forest hardening mechanism. In other words, according to the forest hardening mechanism, the dislocations in the plastic zone that are closer to the indenter are the effective ones. Hence, in the cases of large samples, the most important role of GBs is to change the pattern of the dislocation structure by blocking their movement, which increases the resulting hardness at higher indentation depths. Voyiadjis and Yaghoobi [88] also investigated the effect of GB on the dislocation nucleation and evolution during nanoindentation. For example, Figure 22 depicts the dislocation nucleation and evolution for the $\sum 3\ (1\,1\,1)\ [1\,\bar{1}\,0]$ bicrystal and its related single crystal large samples. Figure 22 supports the underlying mechanism suggested by Voyiadjis and Yaghoobi [88] to capture the effect of GB on the nanoindentation response of large samples. One should note that the strain rates incorporated in the atomistic simulation are much higher than those selected for experiments. Accordingly, the interpretation of the obtained results should be carefully handled. The applied strain rate can influence both hardening mechanisms and dislocation network properties (see, e.g., [140–144]). In other words, one should note that the observed mechanisms are not an artifact of the high strain rates used in the atomistic simulation.

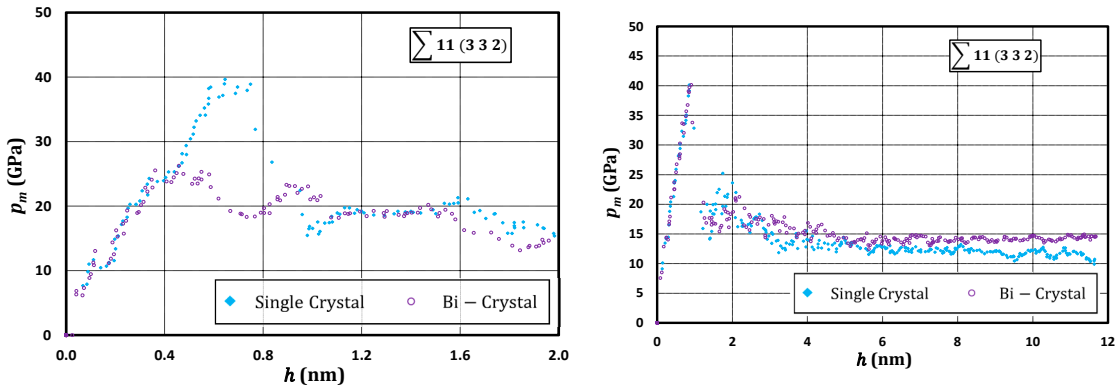

Figure 21. Effect of $\sum 11\ (3\,3\,2)$ grain boundary on the nanoindentation response of Ni thin film: (**a**) small sample and (**b**) large sample (after Voyiadjis and Yaghoobi [88]).

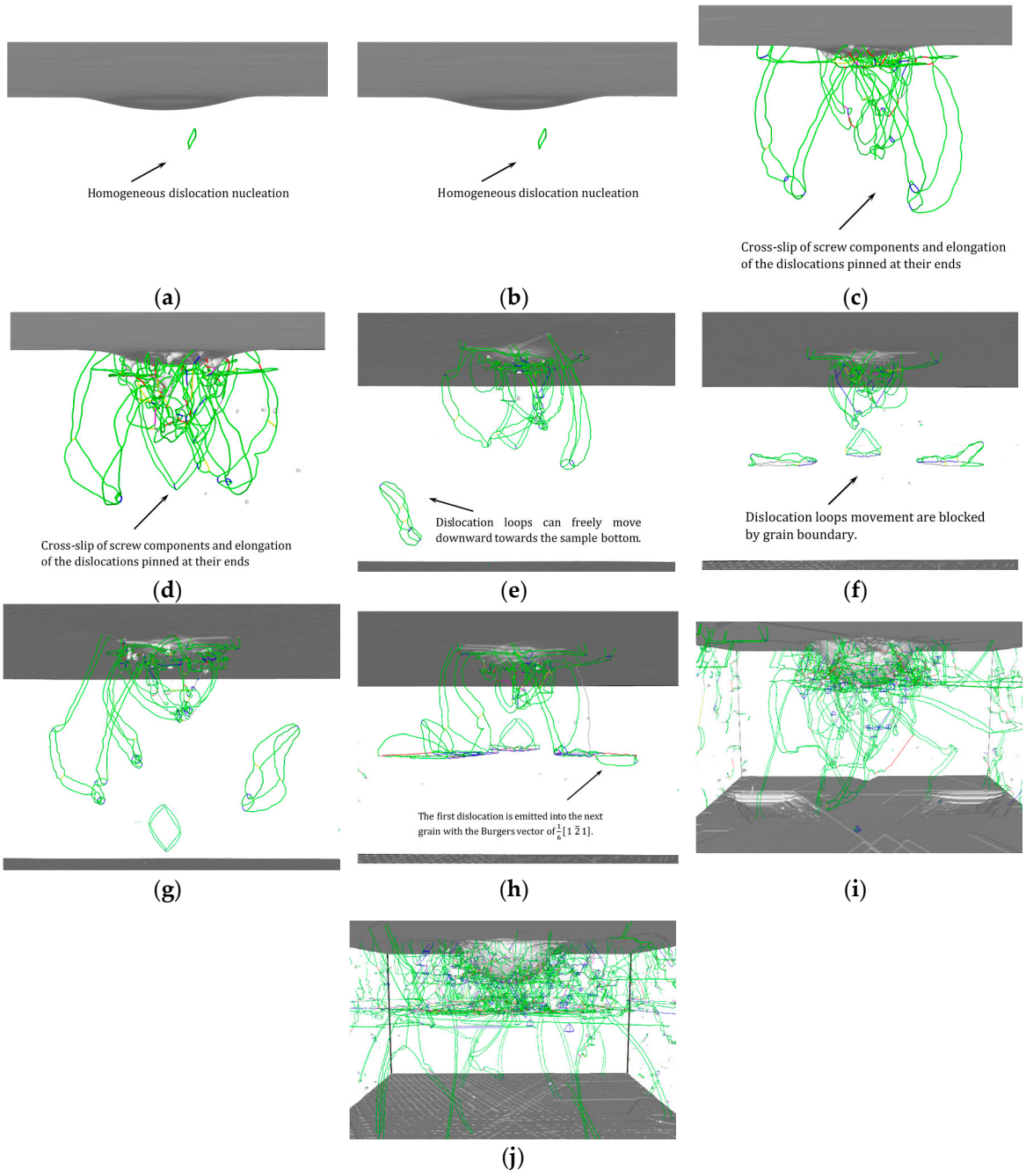

Figure 22. Effect of $\sum 3\,(1\,1\,1)\,\left[1\,\bar{1}\,0\right]$ GB on the dislocation nucleation and evolution of large sample at different indentation depths: (**a**) single crystal sample, $h \approx 0.88$ nm; (**b**) bicrystal sample, $h \approx 0.88$ nm; (**c**) single crystal sample, $h \approx 1.15$ nm; (**d**) bicrystal sample, $h \approx 1.15$ nm; (**e**) single crystal sample, $h \approx 1.44$ nm; (**f**) bicrystal sample, $h \approx 1.44$ nm; (**g**) single crystal sample, $h \approx 2.03$ nm; (**h**) bicrystal sample, $h \approx 2.03$ nm; (**i**) single crystal sample, $h \approx 11.5$ nm; (**j**) bicrystal sample, $h \approx 11.5$ nm (after Voyiadjis and Yaghoobi [88]).

6. Summary and Conclusions

The current work reviews the size effect in crystalline metals during nanoindentation, with emphasis on the underlying mechanisms governing this phenomenon. The indentation size effects in crystalline metals including the variation of hardness versus the indentation depth for geometrically self-similar indenter tips and variation of hardness versus the indenter radius for spherical indenters

are well documented and have been observed by many researchers. The size effects have been successfully captured using the concept of geometrically necessary dislocations (GNDs). Accordingly, the increase in hardness by decreasing the indentation depth is attributed to the increase of GNDs density, which leads to the enhanced strength according to the forest hardening mechanism. A similar methodology has been incorporated to capture the size effects in the case of spherical indenters as the indenter radius varies. Furthermore, a material length scale can be obtained for gradient plasticity models using the same methodology as $l \equiv b(G/\sigma_0)^2$ [13]. The presented mechanism defines the variation of hardness H versus the indentation depth h in the form of $(H/H_0)^2 = 1 + h^*/h$, where H_0 and h^* are the material constants. However, the conducted studies have shown that the developed relation cannot capture the reported size effect for small indentation depths. Furthermore, the coupling effects of indentation depth and grain size effects can be successfully captured using the same methodology. The experimental results show that the grain boundary (GB) may enhance the hardness by blocking the movement of nucleated GNDs. Accordingly, a new material length scale can be obtained for nonlocal plasticity, which incorporates the effect of material grain size [108].

When it comes to the small indentation depths, some discrepancies and contradictory explanations have been presented. The understanding of the underlying mechanisms of size effects during the nanoindentation for shallow indentation depths is becoming more and more complete with the help of extensive experimental and computational investigations. Up to now, three experimental techniques of backscattered electron diffraction (EBSD), convergent beam electron diffraction (CBED) and X-ray microdiffraction (μXRD) have been introduced to measure the dislocation density in metallic samples. These methods have been incorporated to investigate the governing mechanisms of size effects during nanoindentation for small indentation depths. However, two types of trends for the variation of dislocation density have been reported as the indentation depth decreases. Some experimental studies (see, e.g., [95,119,121]) have shown that the dislocation density decreases as the indentation depth decreases, while the hardness increases, which is in contradiction with the conventional size effect theory and its underlying hardening mechanism, i.e., the forest hardening mechanism. The observed hardening as the indentation depth decreases has been attributed to the decrease in the length of dislocation segments. On the other hand, some experimental observations validate the conventional theory of size effects by reporting that the dislocation density increases by decreasing the indentation depth, which increases the hardness according to the forest hardening mechanism (see, e.g., [125]). In the case of small dislocation depths, more experiments need to be conducted to study the nanoindentation size effects by measuring the variation in dislocation density during the indentation and to test which trend is valid, i.e., the dislocation density increases or decreases as the indentation depth decreases. Finally, the atomistic simulation can contribute to the better understanding of the nature of size effects during nanoindentation at smaller indentation depths. The atomistic simulations have investigated many aspects of the nanoindentation response of metallic samples. The dislocation nucleation and evolution can be visualized during the nanoindentation, which can be of great help to investigate the indentation size effect. The conducted simulations have shown that the dislocation density decreases as the indentation depth decreases, while the hardness increases (see, e.g., [87]). The source exhaustion is introduced as the governing mechanism of size effects for shallow indentations where not enough dislocation content is available to sustain the applied plastic flow. Accordingly, as the indentation depth increases, the dislocation density increases, and less stress is required to sustain the plastic flow, which leads to lower hardness. Furthermore, the effect of GB on the indentation size effect can be studied using atomistic simulations. The results have shown that the GB may increase or decrease the indentation hardness depending on the grain size. This is due to the fact that in the case of metallic samples with very fine grains, the GB contributes to the dislocation nucleation, which provides more dislocations at shallow depths and decreases the indentation hardness according to the source exhaustion mechanism. In the case of larger grain sizes, on the other hand, the blockage of dislocation movements by GB enhances the hardness according to the forest hardening mechanism.

Acknowledgments: The current work is partially funded by the NSF EPSCoR CIMM project under Award #OIA-1541079.

Conflicts of Interest: The authors declare no conflict of interest.

References

1. Bull, S.J.; Page, T.F.; Yoffe, E.H. An explanation of the indentation size effect in ceramics. *Philos. Mag. Lett.* **1989**, *59*, 281–288. [CrossRef]
2. Li, H.; Bradt, R.C. The microhardness indentation load/size effect in rutile and cassiterite single crystals. *J. Mater. Sci.* **1993**, *28*, 917–926. [CrossRef]
3. Zhu, T.T.; Bushby, A.J.; Dunstan, D.J. Size effect in the initiation of plasticity for ceramics in nanoindentation. *J. Mech. Phys. Solids* **2008**, *56*, 1170–1185. [CrossRef]
4. Pharr, G.M.; Herbert, E.G.; Gao, Y. The Indentation Size Effect: A Critical Examination of Experimental Observations and Mechanistic Interpretations. *Annu. Rev. Mater. Res.* **2010**, *40*, 271–292. [CrossRef]
5. Mott, B.W. *Microindentation Hardness Testing*; Butterworths: London, UK, 1957.
6. Bückle, H. Progress in microindentation hardness testing. *Metall. Rev.* **1959**, *4*, 49–100. [CrossRef]
7. Gane, N. The direct measurement of the strength of metals on a submicrometer scale. *Proc. R. Soc. Lond. Ser. A* **1970**, *317*, 367–391. [CrossRef]
8. Upit, G.P.; Varchenya, S.A. The size effect in the hardness of single crystals. In *The Science of Hardness Testing and Its Research Applications*; Westbrook, J.H., Conrad, H., Eds.; American Society for Metals: Metals Park, OH, USA, 1973; Volume 10, pp. 135–146.
9. Chen, C.C.; Hendrickson, A.A. Microhardness phenomena in silver. In *The Science of Hardness Testing and Its Research Applications*; Westbrook, J.H., Conrad, H., Eds.; American Society for Metals: Metals Park, OH, USA, 1973; Volume 21, pp. 274–290.
10. Tabor, D. Indentation hardness and its measurement: Some cautionary comments. In *Microindentation Techniques in Materials Science and Engineering. ASTM STP 889*; Blau, P.J., Lawn, B.R., Eds.; ASTM: Philadelphia, PA, USA, 1986; pp. 129–159.
11. Stelmashenko, N.A.; Walls, M.G.; Brown, L.M.; Milman, Y.V. Microindentation on W and Mo oriented single crystals: An STM study. *Acta Metall. Mater.* **1993**, *41*, 2855–2865. [CrossRef]
12. De Guzman, M.S.; Neubauer, G.; Flinn, P.; Nix, W.D. The role of indentation depth on the measured hardness of materials. *Mater. Res. Soc. Symp. Proc.* **1993**, *308*, 613–618. [CrossRef]
13. Nix, W.D.; Gao, H. Indentation size effects in crystalline materials: A law for strain gradient plasticity. *J. Mech. Phys. Solids* **1998**, *46*, 411–425. [CrossRef]
14. Swadener, J.G.; George, E.P.; Pharr, G.M. The correlation of the indentation size effect measured with indenters of various shapes. *J. Mech. Phys. Solids* **2002**, *50*, 681–694. [CrossRef]
15. Lim, Y.Y.; Chaudhri, M.M. The effect of the indenter load on the nanohardness of ductile metals: An experimental study on polycrystalline work-hardened and annealed oxygen-free copper. *Philos. Mag. A* **1999**, *79*, 2979–3000. [CrossRef]
16. Bushby, A.J.; Dunstan, D.J. Plasticity size effects in nanoindentation. *J. Mater. Res.* **2004**, *19*, 137–142. [CrossRef]
17. Spary, I.J.; Bushby, A.J.; Jennett, N.M. On the indentation size effect in spherical indentation. *Phil. Mag.* **2006**, *86*, 5581–5593. [CrossRef]
18. Durst, K.; Göken, M.; Pharr, G.M. Indentation size effect in spherical and pyramidal indentations. *J. Phys. D Appl. Phys.* **2008**, *41*, 074005. [CrossRef]
19. Gerberich, W.W.; Tymiak, N.I.; Grunlan, J.C.; Horstemeyer, M.F.; Baskes, M.I. Interpretations of indentation size effect. *J. Appl. Mech.* **2002**, *69*, 433–442. [CrossRef]
20. Bull, S.J. On the origins of the indentation size effect. *Z. Metallkd.* **2003**, *94*, 787–792. [CrossRef]
21. Zhu, T.T.; Bushby, A.J.; Dunstan, D.J. Materials mechanical size effects: A review. *Mater. Tech.* **2008**, *23*, 193–209. [CrossRef]
22. Kiener, D.; Durst, K.; Rester, M.; Minor, A.M. Revealing deformation mechanisms with nanoindentation. *JOM* **2009**, *61*, 14–23. [CrossRef]
23. Sangwal, K. On the reverse indentation size effect and microhardness measurement of solids. *Mater. Chem. Phys.* **2000**, *63*, 145–152. [CrossRef]

24. King, R.B. Elastic analysis of some punch problems for a layered medium. *Int. J. Solids Struct.* **1987**, *23*, 1657–1664. [CrossRef]
25. Giannakopoulos, A.E.; Larsson, P.L.; Vestergaard, R. Analysis of Vickers indentation. *Int. J. Solids Struct.* **1994**, *31*, 2679–2708. [CrossRef]
26. Larsson, P.L.; Giannakopoulos, A.E.; SÖderlund, E.; Rowcliffe, D.J.; Vestergaard, R. Analysis of Berkovich indentation. *Int. J. Solids Struct.* **1996**, *33*, 221–248. [CrossRef]
27. Bolshakov, A.; Oliver, W.C.; Pharr, G.M. Influences of stress on the measurement of mechanical properties using nanoindentation: Part II. Finite element simulations. *J. Mater. Res.* **1996**, *11*, 760–768. [CrossRef]
28. Bolshakov, A.; Oliver, W.C.; Pharr, G.M. Finite element studies of the influence of pile-up on the analysis of nanoindentation data. *Mater. Res. Soc. Symp. Proc.* **1996**, *436*, 141–146. [CrossRef]
29. Bolshakov, A.; Pharr, G.M. Influences of pileup on the measurement of mechanical properties by load and depth sensing indentation techniques. *J. Mater. Res.* **1998**, *13*, 1049–1058. [CrossRef]
30. Lichinchi, M.; Lenardi, C.; Haupt, J.; Vitali, R. Simulation of Berkovich nanoindentation experiments on thin films using finite element method. *Thin Solid Films* **1998**, *312*, 240–248. [CrossRef]
31. Huber, N.; Tsakmakis, C. Experimental and theoretical investigation of the effect of kinematic hardening on spherical indentation. *Mech. Mater.* **1998**, *27*, 241–248. [CrossRef]
32. Cheng, Y.-T.; Cheng, C.-M.J. Scaling approach to conical indentation in elastic-plastic solids with work hardening. *Appl. Phys.* **1998**, *84*, 1284–1291. [CrossRef]
33. Cheng, Y.-T.; Cheng, C.-M. Scaling relationships in conical indentation of elastic-perfectly plastic solids. *Int. J. Solids Struct.* **1999**, *36*, 1231–1243. [CrossRef]
34. Hay, J.C.; Bolshakov, A.; Pharr, G.M. A critical examination of the fundamental relations used in the analysis of nanoindentation data. *J. Mater. Res.* **1999**, *14*, 2296–2305. [CrossRef]
35. Dao, M.; Chollacoop, N.; Van Vliet, K.J.; Venkatesh, T.A.; Suresh, S. Computational modeling of the forward and reverse problems in instrumented sharp indentation. *Acta Mater.* **2001**, *49*, 3899–3918. [CrossRef]
36. Durst, K.; Backes, B.; Göken, M. Indentation size effect in metallic materials: Correcting for the size of the plastic zone. *Scr. Mater.* **2005**, *52*, 1093–1097. [CrossRef]
37. Warren, A.W.; Guo, Y.B. Machined surface properties determined by nanoindentation: Experimental and FEA studies on the effects of surface integrity and tip geometry. *Surf. Coat. Technol.* **2006**, *201*, 423–433. [CrossRef]
38. Beghini, M.; Bertini, L.; Fontanari, V. Evaluation of the stress–strain curve of metallic materials by spherical indentation. *Int. J. Solids Struct.* **2006**, *43*, 2441–2459. [CrossRef]
39. Walter, C.; Antretter, T.; Daniel, R.; Mitterer, C. Finite element simulation of the effect of surface roughness on nanoindentation of thin films with spherical indenters. *Surf. Coat. Technol.* **2007**, *202*, 1103–1107. [CrossRef]
40. Kalidindi, S.R.; Pathak, S. Determination of the effective zero-point and the extraction of spherical nanoindentation stress–strain curves. *Acta Mater.* **2008**, *56*, 3523–3532. [CrossRef]
41. Sakharova, N.A.; Fernandes, J.V.; Antunes, J.M.; Oliveira, M.C. Comparison between Berkovich, Vickers and conical indentation tests: A three-dimensional numerical simulation study. *Int. J. Solids Struct.* **2009**, *46*, 1095–1104. [CrossRef]
42. Wang, Y.; Raabe, D.; Klüber, C.; Roters, F. Orientation dependence of nanoindentation pile-up patterns and of nanoindentation microtextures in copper single crystals. *Acta Mater.* **2004**, *52*, 2229–2238. [CrossRef]
43. Zaafarani, N.; Raabe, D.; Singh, R.N.; Roters, F.; Zaefferer, S. Three dimensional investigation of the texture and microstructure below a nanoindent in a Cu single crystal using 3D EBSD and crystal plasticity finite element simulations. *Acta Mater.* **2006**, *54*, 1863–1876. [CrossRef]
44. Casals, O.; Očenášek, J.; Alcalá, J. Crystal plasticity finite element simulations of pyramidal indentation in copper single crystals. *Acta Mater.* **2007**, *55*, 55–68. [CrossRef]
45. Zaafarani, N.; Raabe, D.; Roters, F.; Zaefferer, S. On the origin of deformation-induced rotation patterns below nanoindents. *Acta Mater.* **2008**, *56*, 31–42. [CrossRef]
46. Alcalá, J.; Casals, O.; Ocenasek, J. Micromechanics of pyramidal indentation in fcc metals: Single crystal plasticity finite element analysis. *J. Mech. Phys. Solids* **2008**, *56*, 3277–3303. [CrossRef]
47. Britton, T.B.; Liang, H.; Dunne, F.P.E.; Wilkinson, A.J. The effect of crystal orientation on the indentation response of commercially pure titanium: Experiments and simulations. *Proc. R. Soc. Lond. A Math. Phys. Eng. Sci.* **2010**, *466*, 695–719. [CrossRef]

48. Eidel, B. Crystal plasticity finite-element analysis versus experimental results of pyramidal indentation into (001) fcc single crystal. *Acta Mater.* **2011**, *59*, 1761–1771. [CrossRef]
49. Dahlberg, C.F.O.; Saito, Y.; Öztop, M.S.; Kysar, J.W. Geometrically necessary dislocation density measurements associated with different angles of indentations. *Int. J. Plast.* **2014**, *54*, 81–95. [CrossRef]
50. Dahlberg, C.F.O.; Saito, Y.; Öztop, M.S.; Kysar, J.W. Geometrically necessary dislocation density measurements at a grain boundary due to wedge indentation into an aluminum bicrystal. *J. Mech. Phys. Solids* **2017**, *105*, 131–149. [CrossRef]
51. Fivel, M.; Verdier, M.; Canova, G. 3D simulation of a nanoindentation test at a mesoscopic scale. *Mater. Sci. Eng. A* **1997**, *234–236*, 923–926. [CrossRef]
52. Fivel, M.C.; Robertson, C.F.; Canova, G.R.; Boulanger, L. Three-dimensional modeling of indent-induced plastic zone at a mesoscale. *Acta Mater.* **1998**, *46*, 6183–6194. [CrossRef]
53. Kreuzer, H.G.M.; Pippan, R. Discrete dislocation simulation of nanoindentation: The effect of moving conditions and indenter shape. *Mater. Sci. Eng. A* **2004**, *387–389*, 254–256. [CrossRef]
54. Kreuzer, H.G.M.; Pippan, R. Discrete dislocation simulation of nanoindentation. *Comput. Mech.* **2004**, *33*, 292–298. [CrossRef]
55. Kreuzer, H.G.M.; Pippan, R. Discrete dislocation simulation of nanoindentation: Indentation size effect and the influence of slip band orientation. *Acta Mater.* **2004**, *55*, 3229–3235. [CrossRef]
56. Kreuzer, H.G.M.; Pippan, R. Discrete dislocation simulation of nanoindentation: The effect of statistically distributed dislocations. *Mater. Sci. Eng. A* **2005**, *400*, 460–462. [CrossRef]
57. Widjaja, A.; Van Der Giessen, E.; Needleman, A. Discrete dislocation modeling of submicron indentation. *Mater. Sci. Eng. A* **2005**, *400*, 456–459. [CrossRef]
58. Balint, D.S.; Deshpande, V.; Needleman, A.; Van Der Giessen, E. Discrete dislocation plasticity analysis of the wedge indentation of films. *J. Mech. Phys. Solids* **2006**, *54*, 2281–2303. [CrossRef]
59. Widjaja, A.; Van Der Giessen, E.; Deshpande, V.; Needleman, A. Contact area and size effects in discrete dislocation modeling of wedge indentation. *J. Mater. Res.* **2007**, *22*, 655–666. [CrossRef]
60. Rathinam, M.; Thillaigovindan, R.; Paramasivam, P. Nanoindentation of aluminum (100) at various temperatures. *J. Mech. Sci. Technol.* **2009**, *23*, 2652–2657. [CrossRef]
61. Tsuru, T.; Shibutani, Y.; Kaji, Y. Nanoscale contact plasticity of crystalline metal: Experiment and analytical investigation via atomistic and discrete dislocation models. *Acta Mater.* **2010**, *58*, 3096–3102. [CrossRef]
62. Po, G.; Mohamed, M.S.; Crosby, T.; Erel, C.; El-Azab, A.; Ghoniem, N. Recent progress in discrete dislocation dynamics and its applications to micro plasticity. *J. Mater.* **2014**, *66*, 2108–2120. [CrossRef]
63. Tadmor, E.B.; Miller, R.; Philipps, R.; Ortiz, M. Nanoindentation and incipient plasticity. *J. Mater. Res.* **1999**, *14*, 2233–2250. [CrossRef]
64. Smith, G.; Tadmor, E.; Bernstein, N.; Kaxiras, E. Multiscale simulations of silicon nanoindentation. *Acta Mater.* **2001**, *49*, 4089–4101. [CrossRef]
65. Iglesias, R.A.; Leiva, E.P. Two-grain nanoindentation using the quasicontinuum method: Two-dimensional model approach. *Acta Mater.* **2006**, *54*, 2655–2664. [CrossRef]
66. Fanlin, Z.; Yi, S. Quasicontinuum simulation of nanoindentation of nickel film. *Acta Mech. Solida Sin.* **2006**, *19*, 283–288. [CrossRef]
67. Jin, J.; Shevlin, S.; Guo, Z. Multiscale simulation of onset plasticity during nanoindentation of Al (001) surface. *Acta Mater.* **2008**, *56*, 4358–4368. [CrossRef]
68. Jiang, W.G.; Su, J.J.; Feng, X.Q. Effect of surface roughness on nanoindentation test of thin films. *Eng. Fract. Mech.* **2008**, *75*, 4965–4972. [CrossRef]
69. Li, J.; Ni, Y.; Wang, H.; Mei, J. Effects of crystalline anisotropy and indenter size on nanoindentation by multiscale simulation. *Nanoscale Res. Lett.* **2009**, *5*, 420–432. [CrossRef] [PubMed]
70. Yu, W.; Shen, S. Effects of small indenter size and its position on incipient yield loading during nanoindentation. *Mater. Sci. Eng. A* **2009**, *526*, 211–218. [CrossRef]
71. Yu, W.; Shen, S. Multiscale analysis of the effects of nanocavity on nanoindentation. *Comput. Mater. Sci.* **2009**, *46*, 425–430. [CrossRef]
72. Yu, W.; Shen, S. Initial dislocation topologies of nanoindentation into copper (001) film with a nanocavity. *Eng. Fract. Mech.* **2010**, *77*, 3329–3340. [CrossRef]
73. Li, J.; Lu, H.; Ni, Y.; Mei, J. Quasicontinuum study the influence of misfit dislocation interactions on nanoindentation. *Comput. Mater. Sci.* **2011**, *50*, 3162–3170. [CrossRef]

74. Lu, H.; Li, J.; Ni, Y. Position effect of cylindrical indenter on nanoindentation into Cu thin film by multiscale analysis. *Comput. Mater. Sci.* **2011**, *50*, 2987–2992. [CrossRef]
75. Lu, H.; Ni, Y. Effect of surface step on nanoindentation of thin films by multiscale analysis. *Thin Solid Films* **2012**, *520*, 4934–4940. [CrossRef]
76. Lu, H.; Ni, Y.; Mei, J.; Li, J.; Wang, H. Anisotropic plastic deformation beneath surface step during nanoindentation of fcc al by multiscale analysis. *Comput. Mater. Sci.* **2012**, *58*, 192–200. [CrossRef]
77. Landman, U.; Luedtke, W.; Burnham, N.A.; Colton, R.J. Atomistic mechanisms and dynamics of adhesion, nanoindentation, and fracture. *Science* **1990**, *248*, 454–461. [CrossRef] [PubMed]
78. Hoover, W.G.; De Groot, A.J.; Hoover, C.G.; Stowers, I.F.; Kawai, T.; Holian, B.L.; Boku, T.; Ihara, S.; Belak, J. Large-scale elastic-plastic indentation simulations via nonequilibrium molecular dynamics. *Phys. Rev. A* **1990**, *42*, 5844–5853. [CrossRef] [PubMed]
79. Kelchner, C.L.; Plimpton, S.J.; Hamilton, J.C. Dislocation nucleation and defect structure during surface indentation. *Phys. Rev. B* **1998**, *58*, 11085–11088. [CrossRef]
80. Zimmerman, J.A.; Kelchner, C.L.; Klein, P.A.; Hamilton, J.C.; Foiles, S.M. Surface step effects on nanoindentation. *Phys. Rev. Lett.* **2001**, *87*, 165507. [CrossRef] [PubMed]
81. Li, J.; Van Vliet, K.J.; Zhu, T.; Yip, S.; Suresh, S. Atomistic mechanisms governing elastic limit and incipient plasticity in crystals. *Nature* **2002**, *418*, 307–310. [CrossRef] [PubMed]
82. Zhu, T.; Li, J.; Van Vliet, K.J.; Ogata, S.; Yip, S.; Suresh, S.J. Predictive modeling of nanoindentation-induced homogeneous dislocation nucleation in copper. *J. Mech. Phys. Solids* **2004**, *52*, 691–724. [CrossRef]
83. Lee, Y.; Park, J.Y.; Kim, S.Y.; Jun, S. Atomistic simulations of incipient plasticity under Al (111) nanoindentation. *Mech. Mater.* **2005**, *37*, 1035–1048. [CrossRef]
84. Jang, H.; Farkas, D. Interaction of lattice dislocations with a grain boundary during nanoindentation simulation. *Mater. Lett.* **2007**, *61*, 868–871. [CrossRef]
85. Yaghoobi, M.; Voyiadjis, G.Z. Effect of boundary conditions on the MD simulation of nanoindentation. *Comput. Mater. Sci.* **2014**, *95*, 626–636. [CrossRef]
86. Voyiadjis, G.Z.; Yaghoobi, M. Large scale atomistic simulation of size effects during nanoindentation: Dislocation length and hardness. *Mater. Sci. Eng. A* **2015**, *634*, 20–31. [CrossRef]
87. Yaghoobi, M.; Voyiadjis, G.Z. Atomistic simulation of size effects in single-crystalline metals of confined volumes during nanoindentation. *Comput. Mater. Sci.* **2016**, *111*, 64–73. [CrossRef]
88. Voyiadjis, G.Z.; Yaghoobi, M. Role of grain boundary on the sources of size effects. *Comput. Mater. Sci.* **2016**, *117*, 315–329. [CrossRef]
89. Ashby, M.F. The deformation of plastically non-homogeneous materials. *Philos. Mag.* **1970**, *21*, 399–424. [CrossRef]
90. Pugno, N.M. A general shape/size-effect law for nanoindentation. *Acta Mater.* **2007**, *55*, 1947–1953. [CrossRef]
91. Ma, Q.; Clarke, D.R. Size dependent hardness of silver single crystals. *J. Mater. Res.* **1995**, *10*, 853–863. [CrossRef]
92. Poole, W.J.; Ashby, M.F.; Fleck, N.A. Micro-hardness of annealed and work-hardened copper polycrystals. *Scr. Mater.* **1996**, *34*, 559–564. [CrossRef]
93. McElhaney, K.W.; Valssak, J.J.; Nix, W.D. Determination of indenter tip geometry and indentation contact area for depth sensing indentation experiments. *J. Mater. Res.* **1998**, *13*, 1300–1306. [CrossRef]
94. Liu, Y.; Ngan, A.H.W. Depth dependence of hardness in copper single crystals measured by nanoindentation. *Scr. Mater.* **2001**, *44*, 237–241. [CrossRef]
95. McLaughlin, K.K.; Clegg, W.J. Deformation underneath low-load indentations in copper. *J. Phys. D* **2008**, *41*, 074007. [CrossRef]
96. Rester, M.; Motz, C.; Pippan, R. Indentation across size scales: A survey of indentation-induced plastic zones in copper {111} single crystals. *Scr. Mater.* **2008**, *59*, 742–745. [CrossRef]
97. Abu Al-Rub, R.K.; Voyiadjis, G.Z. Analytical and experimental determination of the material intrinsic length scale of strain gradient plasticity theory from micro- and nano-indentation experiments. *Int. J. Plast.* **2004**, *20*, 1139–1182. [CrossRef]
98. Feng, G.; Nix, W.D. Indentation size effect in MgO. *Scr. Mater.* **2004**, *51*, 599–603. [CrossRef]
99. Huang, Y.; Zhang, F.; Hwang, K.C.; Nix, W.D.; Pharr, G.M.; Feng, G. A model for size effects in nanoindentation. *J. Mech. Phys. Solids* **2006**, *54*, 1668–1686. [CrossRef]

100. Soer, W.A.; De Hosson, J.T.M. Detection of grain-boundary resistance to slip transfer using nanoindentation. *Mater. Lett.* **2005**, *59*, 3192–3195. [CrossRef]
101. Cao, Y.; Allameh, S.; Nankivil, D.; Sethiaraj, S.; Otiti, T.; Soboyejo, W. Nanoindentation measurements of the mechanical properties of polycrystalline Au and Ag thin films on silicon substrates: Effects of grain size and film thickness. *Mater. Sci. Eng. A* **2006**, *427*, 232–240. [CrossRef]
102. Hou, X.D.; Bushby, A.J.; Jennett, N.M. Study of the interaction between the indentation size effect and Hall–Petch effect with spherical indenters on annealed polycrystalline copper. *J. Phys. D Appl. Phys.* **2008**, *41*, 074006. [CrossRef]
103. Voyiadjis, G.Z.; Peters, R. Size effects in nanoindentation: An experimental and analytical study. *Acta Mech.* **2010**, *211*, 131–153. [CrossRef]
104. Voyiadjis, G.Z.; Almasri, A.H.; Park, T. Experimental nanoindentation of BCC metals. *Mech. Res. Commun.* **2010**, *37*, 307–314. [CrossRef]
105. Almasri, A.H.; Voyiadjis, G.Z. Nano-indentation in FCC metals: Experimental study. *Acta Mech.* **2010**, *209*, 1–9. [CrossRef]
106. Voyiadjis, G.Z.; Faghihi, D.; Zhang, C. Analytical and experimental determination of rate-and temperature-dependent length scales using nanoindentation experiments. *J. Nanomech. Micromech.* **2011**, *1*, 24–40. [CrossRef]
107. Voyiadjis, G.Z.; Zhang, C. The mechanical behavior during nanoindentation near the grain boundary in a bicrystal FCC metal. *Mater. Sci. Eng. A* **2015**, *621*, 218–228. [CrossRef]
108. Zhang, C.; Voyiadjis, G.Z. Rate-dependent size effects and material length scales in nanoindentation near the grain boundary for a bicrystal FCC metal. *Mater. Sci. Eng. A* **2016**, *659*, 55–62. [CrossRef]
109. Voyiadjis, G.Z.; Abu Al-Rub, R.K. Gradient Plasticity Theory with a Variable Length Scale Parameter. *Int. J. Solids Struct.* **2005**, *42*, 3998–4029. [CrossRef]
110. Uchic, M.D.; Dimiduk, D.M.; Florando, J.N.; Nix, W.D. Exploring specimen size effects in plastic deformation of Ni3(Al,Ta). *Mater. Res. Soc. Symp. Proc.* **2003**, *753*, 27–32. [CrossRef]
111. Uchic, M.D.; Dimiduk, D.M.; Florando, J.N.; Nix, W.D. Sample dimensions influence strength and crystal plasticity. *Science* **2004**, *305*, 986–989. [CrossRef] [PubMed]
112. Uchic, M.D.; Shade, P.A.; Dimiduk, D.M. Plasticity of micrometer-scale single crystals in compression. *Annu. Rev. Mater. Res.* **2009**, *39*, 361–386. [CrossRef]
113. Kraft, O.; Gruber, P.; Mönig, R.; Weygand, D. Plasticity in confined dimensions. *Annu. Rev. Mater. Res.* **2010**, *40*, 293–317. [CrossRef]
114. Parthasarathy, T.A.; Rao, S.I.; Dimiduk, D.M.; Uchic, M.D.; Trinkle, D.R. Contribution to size effect of yield strength from the stochastics of dislocation source lengths in finite samples. *Scr. Mater.* **2007**, *56*, 313–316. [CrossRef]
115. Rao, S.I.; Dimiduk, D.M.; Tang, M.; Parthasarathy, T.A.; Uchic, M.D.; Woodward, C. Estimating the strength of single-ended dislocation sources in micron-sized single crystals. *Philos. Mag.* **2007**, *87*, 4777–4794. [CrossRef]
116. Norfleet, D.M.; Dimiduk, D.M.; Polasik, S.J.; Uchic, M.D.; Mills, M.J. Dislocation structures and their relationship to strength in deformed nickel microcrystals. *Acta Mater.* **2008**, *56*, 2988–3001. [CrossRef]
117. Rao, S.I.; Dimiduk, D.M.; Parthasarathy, T.A.; Uchic, M.D.; Tang, M.; Woodward, C. Athermal mechanisms of size-dependent crystal flow gleaned from three-dimensional discrete dislocation simulations. *Acta Mater.* **2008**, *56*, 3245–3259. [CrossRef]
118. Greer, J.R.; Oliver, W.C.; Nix, W.D. Size dependence of mechanical properties of gold at the micron scale in the absence of strain gradients. *Acta Mater.* **2005**, *53*, 1821–1830. [CrossRef]
119. Kiener, D.; Pippan, R.; Motz, C.; Kreuzer, H. Microstructural evolution of the deformed volume beneath microindents in tungsten and copper. *Acta Mater.* **2006**, *54*, 2801–2811. [CrossRef]
120. Rester, M.; Motz, C.; Pippan, R. Microstructural investigation of the volume beneath nanoindentations in copper. *Acta Mater.* **2007**, *55*, 6427–6435. [CrossRef]
121. Demir, E.; Raabe, D.; Zaafarani, N.; Zaefferer, S. Investigation of the indentation size effect through the measurement of the geometrically necessary dislocations beneath small indents of different depths using EBSD tomography. *Acta Mater.* **2009**, *57*, 559–569. [CrossRef]
122. Yang, W.; Larson, B.C.; Pharr, G.M.; Ice, G.E.; Budai, J.D.; Tischler, J.Z.; Liu, W. Deformation microstructure under microindents in single-crystal Cu using three-dimensional X-ray structural microscopy. *J. Mater. Res.* **2004**, *19*, 66–72. [CrossRef]

123. Larson, B.C.; El-Azab, A.; Yang, W.; Tischler, J.Z.; Liu, W.; Ice, G.E. Experimental characterization of the mesoscale dislocation density tensor. *Philos. Mag.* **2007**, *87*, 1327–1347. [CrossRef]
124. Larson, B.C.; Tischler, J.Z.; El-Azab, A.; Liu, W. Dislocation density tensor characterization of deformation using 3D X-ray microscopy. *J. Eng. Mater. Technol.* **2008**, *130*, 021024. [CrossRef]
125. Feng, G.; Budiman, A.S.; Nix, W.D.; Tamura, N.; Patel, J.R. Indentation size effects in single crystal copper as revealed by synchrotron X-ray microdiffraction. *J. Appl. Phys.* **2008**, *104*, 043501. [CrossRef]
126. Hasnaoui, A.; Derlet, P.M.; Van Swygenhoven, H. Interaction between dislocations and grain boundaries under an indenter–a molecular dynamics simulation. *Acta Mater.* **2004**, *52*, 2251–2258. [CrossRef]
127. Kulkarni, Y.; Asaroa, R.J.; Farkas, D. Are nanotwinned structures in fcc metals optimal for strength, ductility and grain stability? *Scr. Mater.* **2009**, *60*, 532–535. [CrossRef]
128. Nair, A.K.; Parker, E.; Gaudreau, P.; Farkas, D.; Kriz, R.D. Size effects in indentation response of thin films at the nanoscale: A molecular dynamics study. *Int. J. Plast.* **2008**, *24*, 2016–2031. [CrossRef]
129. Peng, P.; Liao, G.; Shi, T.; Tang, Z.; Gao, Y. Molecular dynamic simulations of nanoindentation in aluminum thin film on silicon substrate. *Appl. Surf. Sci.* **2010**, *256*, 6284–6290. [CrossRef]
130. Sun, K.; Shen, W.; Ma, L. The influence of residual stress on incipient plasticity in single-crystal copper thin film under nanoindentation. *Comput. Mater. Sci.* **2014**, *81*, 226–232. [CrossRef]
131. Szlufarska, I. Atomistic simulations of nanoindentation. *Mater. Today* **2006**, *9*, 42–50. [CrossRef]
132. Daw, M.S.; Baskes, M.I. Embedded-atom method: Derivation and application to impurities, surfaces, and other defects in metals. *Phys. Rev. B* **1984**, *29*, 6443–6453. [CrossRef]
133. Baskes, M.I. Modified embedded-atom potentials for cubic materials and impurities. *Phys. Rev. B* **1992**, *46*, 2727–2742. [CrossRef]
134. Medyanik, S.N.; Shao, S. Strengthening effects of coherent interfaces in nanoscale metallic bilayers. *Comput. Mater. Sci.* **2009**, *45*, 1129–1133. [CrossRef]
135. Shao, S.; Medyanik, S.N. Dislocation–interface interaction in nanoscale fcc metallic bilayers. *Mech. Res. Commun.* **2010**, *37*, 315–319. [CrossRef]
136. Saraev, D.; Miller, R.E. Atomic-scale simulations of nanoindentation-induced plasticity in copper crystals with nanometer-sized nickel coatings. *Acta Mater.* **2006**, *54*, 33–45. [CrossRef]
137. Stukowski, A. Structure identification methods for atomistic simulations of crystalline materials. *Model. Simul. Mater. Sci. Eng.* **2012**, *20*, 045021. [CrossRef]
138. Stukowski, A.; Albe, K. Extracting dislocations and non-dislocation crystal defects from atomistic simulation data. *Model. Simul. Mater. Sci. Eng.* **2010**, *18*, 085001. [CrossRef]
139. Gao, Y.; Ruestes, C.J.; Tramontina, D.R.; Urbassek, H.M. Comparative simulation study of the structure of the plastic zone produced by nanoindentation. *J. Mech. Phys. Solids* **2015**, *75*, 58–75. [CrossRef]
140. Armstrong, R.W.; Walley, S.M. High strain rate properties of metals and alloys. *Int. Mater. Rev.* **2008**, *53*, 105–128. [CrossRef]
141. Armstrong, R.W.; Li, Q. Dislocation mechanics of high-rate deformations. *Metall. Mater. Trans. A* **2015**, *46*, 4438–4453. [CrossRef]
142. Yaghoobi, M.; Voyiadjis, G.Z. Size Effects in FCC Crystals During the High Rate Compression Test. *Acta Mater.* **2016**, *121*, 190–201. [CrossRef]
143. Voyiadjis, G.Z.; Yaghoobi, M. Size and Strain Rate Effects in Metallic Samples of Confined Volumes: Dislocation Length Distribution. *Scr. Mater.* **2017**, *130*, 182–186. [CrossRef]
144. Yaghoobi, M.; Voyiadjis, G.Z. Microstructural investigation of the hardening mechanism in FCC crystals during high rate deformations. *Comput. Mater. Sci.* **2017**, *138*, 10–15. [CrossRef]

© 2017 by the authors. Licensee MDPI, Basel, Switzerland. This article is an open access article distributed under the terms and conditions of the Creative Commons Attribution (CC BY) license (http://creativecommons.org/licenses/by/4.0/).